

# Impacts of Atmospheric Reanalysis Uncertainty on Atlantic Overturning Estimates at 25°N

HELEN R. PILLAR<sup>a</sup> AND HELEN L. JOHNSON

*Department of Earth Sciences, University of Oxford, Oxford, United Kingdom*

DAVID P. MARSHALL

*Department of Physics, University of Oxford, Oxford, United Kingdom*

PATRICK HEIMBACH

*Institute for Computational Engineering and Sciences, The University of Texas at Austin, Austin, Texas*

SO TAKAO

*Imperial College London, London, United Kingdom*

(Manuscript received 20 April 2018, in final form 18 July 2018)

## ABSTRACT


Atmospheric reanalyses are commonly used to force numerical ocean models, but despite large discrepancies reported between different products, the impact of reanalysis uncertainty on the simulated ocean state is rarely assessed. In this study, the impact of uncertainty in surface fluxes of buoyancy and momentum on the modeled Atlantic meridional overturning at 25°N is quantified for the period January 1994–December 2011. By using an ocean-only climate model and its adjoint, the space and time origins of overturning uncertainty resulting from air–sea flux uncertainty are fully explored. Uncertainty in overturning induced by prior air–sea flux uncertainty can exceed 4 Sv (where 1 Sv  $\equiv 10^6 \text{ m}^3 \text{ s}^{-1}$ ) within 15 yr, at times exceeding the amplitude of the ensemble-mean overturning anomaly. A key result is that, on average, uncertainty in the overturning at 25°N is dominated by uncertainty in the zonal wind at lags of up to 6.5 yr and by uncertainty in surface heat fluxes thereafter, with winter heat flux uncertainty over the Labrador Sea appearing to play a critically important role.


## 1. Introduction

Ocean general circulation models (OGCMs) are an important tool in climate research. Although fully coupled Earth system models—with interacting physical, biogeochemical, and ecosystem components—are now

commonly used for twenty-first-century prediction studies, OGCMs remain extremely valuable for exploring the ocean's role in shaping Earth's climate. This value lies in both the reduced computational cost and reduced complexity of ocean-only model configurations. Both of these factors facilitate thorough mechanistic investigations of processes controlling the mean state and variability of the global ocean circulation.

Omission of an interactive atmosphere in OGCMs demands specification of the air–sea fluxes of buoyancy and momentum at the surface boundary. These fluxes can be obtained directly from atmospheric reanalyses or computed in the OGCM via bulk formula (e.g., Large and Pond 1981; Large and Yeager 2004), with the latter

 Denotes content that is immediately available upon publication as open access.

 Supplemental information related to this paper is available at the Journals Online website: <https://doi.org/10.1175/JCLI-D-18-0241.s1>.

<sup>a</sup> Current affiliation: Institute for Computational Engineering and Sciences, The University of Texas at Austin, Austin, Texas.

*Corresponding author:* Helen Pillar, [helen.pillar@utexas.edu](mailto:helen.pillar@utexas.edu)



This article is licensed under a [Creative Commons Attribution 4.0 license](http://creativecommons.org/licenses/by/4.0/) (<http://creativecommons.org/licenses/by/4.0/>).

requiring reanalyzed estimates of near-surface atmospheric fields. Several operational centers now produce multidecadal reanalyzed atmospheric datasets, including the European Centre for Medium-Range Weather Forecasts (Uppala et al. 2005; Dee et al. 2011), the National Centers for Environmental Prediction (Kalnay et al. 1996; Kanamitsu et al. 2002), and the Japan Meteorological Agency (Ebita et al. 2011; Kobayashi et al. 2015).

In this paper, we assess how uncertainty in the reanalyzed air–sea flux estimates provided by different agencies impacts the circulation in an OGCM. We focus on the impacts on variability in the monthly mean Atlantic meridional overturning circulation (AMOC) at 25°N (hereafter referred to as  $AMOC_{25N}$ ). Our choice of metric is motivated by a vast body of work linking AMOC variations to low-frequency changes in North Atlantic surface temperatures (e.g., Delworth and Mann 2000; Knight et al. 2005; Zhang and Delworth 2005; Klöwer et al. 2014), with far-reaching impacts on regional and global climate (see review by Buckley and Marshall 2016, and references therein). Importantly, there is growing support for the potential predictability of the North Atlantic climate on decadal time scales (e.g., Robson et al. 2012a,b; Yeager et al. 2015; Årthun et al. 2017), arising from the long memory and meridional connectivity of the AMOC. Latitudes near 25°N are of particular interest as there have been significant past and ongoing efforts to monitor the basinwide circulation here (Cunningham et al. 2007; McCarthy et al. 2015). Furthermore, previous studies support that much of the variability observed in  $AMOC_{25N}$  is due to external forcing (Roberts et al. 2013; Pillar et al. 2016) as opposed to internal variability, suggesting air–sea flux uncertainty may also play an important role in driving modeled  $AMOC_{25N}$  uncertainty.

The impact of air–sea flux uncertainty on the modeled ocean state can be explored by forcing an OGCM with an ensemble of atmospheric reanalyses and measuring the divergence in modeled transport (existing studies will be reviewed in the next section). Here, we take a different approach by projecting an ensemble of reanalyzed air–sea fluxes onto time-evolving maps of the linearized sensitivity of  $AMOC_{25N}$  to air–sea exchange of buoyancy and momentum (Czeschel et al. 2010; Heimbach et al. 2011; Pillar et al. 2016). These sensitivity maps are computed using an OGCM and its adjoint. By using the adjoint we can unambiguously quantify separate contributions from the uncertainty in surface fluxes of freshwater, heat, zonal momentum, and meridional momentum to the total uncertainty in the modeled  $AMOC_{25N}$ . Furthermore, we can identify the exact time and space origins of the air–sea flux uncertainty dominating uncertainty in the modeled

$AMOC_{25N}$ . This allows us to examine how  $AMOC_{25N}$  uncertainty evolves with time and explore whether there is a difference between where and when the reanalysis air–sea flux uncertainty is largest and where and when this uncertainty has the largest impact on the modeled  $AMOC_{25N}$ .

The paper is organized as follows. In section 2 we present a background discussion of the atmospheric reanalysis procedure. In section 3 we describe the derivation of  $AMOC_{25N}$  adjoint-based sensitivities and the selection of the atmospheric reanalysis ensemble. In section 4 we identify when and where reanalysis uncertainty has the largest impact on  $AMOC_{25N}$ . We identify critical reductions in air–sea flux uncertainty for improved modeling of  $AMOC_{25N}$  in section 5. Our discussion and conclusions are presented in section 6.

## 2. Background

Global atmospheric reanalyses are produced by reprocessing millions of archived atmospheric observations using a state-of-the-art weather forecasting system. This reprocessing involves deriving the best estimate of the atmospheric state over sequential short (typically 1 day) analysis cycles nested within the full (typically multidecadal) reanalysis period. For each analysis cycle, a prior estimate of the atmospheric state is first provided from a model forecast initialized at the end of the previous cycle. The misfit between the prior estimate and the observations, which are irregularly distributed in space and time, is then computed and used to inform adjustments to the model state and/or parameters for minimization of this misfit. The forecast is then rerun to provide a corrected estimate of the atmospheric state. Repeating this procedure for consecutive analysis cycles yields continuous multidecadal gridded records of both directly observed and derived variables. They are easy to handle and frequently updated, and have been used extensively to investigate atmospheric variability and force OGCMs.

It is critical to note that sequential assimilation procedures [see Stammer et al. (2016) for a review of different methodologies] reduce model–observation misfit by applying time-varying corrections to elements of the model. These corrections can violate conservation principles, complicating the use of reanalyses in climate research (Wunsch and Heimbach 2013a; Stammer et al. 2016). For example, large imbalances of surface heat and freshwater present in reanalyses (Wunsch and Heimbach 2013a) are not supported by observed changes in ocean storage (Levitus et al. 2012). Furthermore, continual expansion of the observational network (Dee 2005; Bengtsson et al. 2007; Thorne and Vose 2010;

Dessler and Davis 2010) and changes in instrumentation during the reanalysis period (Thompson et al. 2008; Simmons et al. 2010) diminish the model and observational biases, which manifests as a spurious low-frequency trend in the reanalysis (Bengtsson et al. 2004a,b; Santer et al. 2004). This is associated most notably with the advent of meteorological satellites, when many reanalyzed variables exhibit a step change in mean value (e.g., Pawson and Fiorino 1999; Santer et al. 1999; Wunsch and Heimbach 2013a). Recognizing this issue, reanalyses spanning the twentieth century assimilate only surface pressure reports [e.g., NOAA–CIRES Twentieth Century Reanalysis (20CR); Compo et al. 2011], which have been regularly produced since the late 1800s. Despite progress in the direction of “bias aware” assimilation to detect and correct reanalysis bias arising from deficiencies in the atmospheric model, observational operators, and error covariance assumptions (Dee 2005), systematic errors remain challenging to remove.

As highlighted by Wunsch and Heimbach (2013a), all reanalysis products are a synthesis of uncertain observations and imperfect models, yet many are used without acknowledgment of the entailed error. Error estimates can be obtained by comparing reanalysis products to independent, unassimilated observations or intercomparing an ensemble of reanalyses. Direct comparison with unassimilated observations yields the most accurate estimates of the absolute error, but is typically limited in space and time. Intercomparison between reanalyses is useful for probing the full space and time structure of differences between products, but masks shared biases. A combined approach (e.g., Chaudhuri et al. 2013; Brunke et al. 2011), using multiple reanalysis products, yields the most comprehensive assessment of reanalysis uncertainty. These studies have highlighted particularly severe errors in all reanalyzed wind stress and precipitation fields, due to uncertainties in computing the stress from the observed speed and poor model representation of the cloud physics, respectively. The different geographical distributions of time-mean and time-varying air–sea flux biases have also been noted (Chaudhuri et al. 2013), but the impact of the identified biases on the modeled ocean state remains to be fully explored.

Chaudhuri et al. (2016) compare 10-yr-long integrations of a coarse-resolution global configuration of the Massachusetts Institute of Technology general circulation model (MITgcm; Marshall et al. 1997a,b) forced by four different reanalysis products. By comparing the ensemble spread with observed model–data misfits, they estimate the fraction of model error that may be attributable to forcing uncertainty. The authors find that model biases in tropical SST and sea level may

be largely explained by uncertainties in the reanalysis forcing. Forcing uncertainty is also shown to have a notable impact on the modeled Southern Ocean circulation, generating uncertainties of  $\sim 5$  and  $\sim 1.5$  Sv (where  $1 \text{ Sv} \equiv 10^6 \text{ m}^3 \text{ s}^{-1}$ ) in the barotropic streamfunction close to Antarctica and in the meridional overturning streamfunction, respectively. Although the authors map the model error fraction explained by forcing uncertainty for many variables, it is important to note that the relevant forcing uncertainty may be nonlocal.

Assessments of the relative importance of uncertainty in air–sea fluxes of buoyancy and momentum have been presented by Brodeau et al. (2010) and He et al. (2016), both comparing two flux products. Brodeau et al. (2010) examined 47-yr-long integrations of a coarse-resolution global configuration of the NEMO OGCM forced by two different reanalysis-based surface datasets; COREv1 (Large and Yeager 2004) and Drakkar Forcing Set 3 (DFS3; Brodeau et al. 2010). The authors show that the AMOC is 2 Sv stronger in the DFS3-forced integration, relative to the COREv1-forced integration. Experiments with mixed COREv1–DFS3 forcings indicate that this strengthening is due to enhanced air–sea buoyancy fluxes over the Nordic Seas and the northern North Atlantic in DFS3. A similar investigation by He et al. (2016) examined the difference in the AMOC forced by COREv2 (Large and Yeager 2009) and 20CR (Compo et al. 2011) air–sea fluxes. They identify wind forcing uncertainty to be critical in causing AMOC uncertainties as large as 3 Sv. A small set of additional experiments with mixed COREv2–20CR forcings highlights the dominance of uncertainty in winds over the North Atlantic and Arctic. However, with this forward modeling approach, it is difficult to unambiguously determine exactly when in time and where in space uncertainties in each forcing field have the largest impact on the modeled AMOC. A key aim of this paper is to identify the time and space origins of the surface buoyancy and momentum flux uncertainties dominating uncertainty in the externally forced  $\text{AMOC}_{25\text{N}}$ . We now describe how we designed our experiment to achieve this aim.

### 3. Experiment design

This study is an extension of our recent investigation into the attribution of observed  $\text{AMOC}_{25\text{N}}$  variability to past surface forcing (Pillar et al. 2016). In that earlier study, we provided quantitative estimates of wind and buoyancy-driven  $\text{AMOC}_{25\text{N}}$  variations over the last 15 yr by projecting air–sea fluxes from the NCEP–DOE AMIP-II reanalysis (hereafter referred to as NCEPII; Kanamitsu et al. 2002) onto model-based dynamical patterns of  $\text{AMOC}_{25\text{N}}$  sensitivity to surface wind, thermal,

and freshwater forcing. Here, we repeat the projection for four additional atmospheric reanalysis products to estimate the error in modeled AMOC<sub>25N</sub> arising from uncertainty in the surface forcing. The model configuration and sensitivity calculation are identical to those described in Pillar et al. (2016) and are briefly reviewed below before the reanalysis ensemble is discussed.

### a. Model configuration

We use a  $1^\circ \times 1^\circ$  ocean-only configuration of the MITgcm, with realistic bathymetry, truncated below the poles at  $78^\circ\text{S}$  and  $74^\circ\text{N}$ . In the vertical there are 33 levels with thickness increasing from 10 m at the surface to 250 m in the abyss. The ocean model is driven by provision of a 12-month repeating cycle of climatological mean air–sea heat ( $Q$ ), freshwater ( $E - P$ ), and momentum ( $[\tau^x, \tau^y]$ ) fluxes from NCEP II and runoff ( $R$ ) from the Ocean Model Intercomparison Project (OMIP) forcing dataset. The latter includes modifications from Dai and Trenberth (2002). The NCEP II climatology is computed using reanalyzed fluxes from January 1979 to June 2015. The runoff climatology is computed from the single year of daily values provided by OMIP. A closure correction is applied to both the heat and freshwater fluxes to ensure no net input over the annual cycle.

Initial temperature and salinity values are horizontally averaged climatologies from the *World Ocean Atlas* (Locarnini et al. 2010; Antonov et al. 2010). To prevent significant drift of sea surface temperature and salinity, we relax to observed climatology with damping time scales of 2 and 6 months, respectively. Restoration of the full-depth temperature and salinity fields toward observed climatology is also imposed at the open northern boundary. Advection and diffusion of tracers along isopycnals by unresolved geostrophic eddies are parameterized using the Gent and McWilliams (1990) and Redi (1982) schemes, respectively. Subgrid-scale vertical mixing is parameterized using the  $K$ -profile parameterization (KPP) scheme (Large et al. 1994). A more detailed description of the model configuration, including a list of key model parameters, is given in Pillar (2013).

Following integration over 1300 model years no significant trends are discernible in the tracer and momentum fields and equilibrium is assumed. The steady-state AMOC<sub>25N</sub> has an annual mean of  $\sim 21$  Sv and a seasonal cycle of 4 Sv in peak-to-peak amplitude. Decadal variability in AMOC<sub>25N</sub> is also visible but is weak relative to the seasonal cycle.

### b. AMOC<sub>25N</sub> sensitivity estimation

Time-evolving maps of AMOC<sub>25N</sub> linear sensitivity to surface wind, and thermal and freshwater fluxes, are computed using the adjoint of the MITgcm (e.g., Marotzke and

Scott 1999; Heimbach et al. 2005) and presented in our earlier study (Pillar et al. 2016). This is achieved by integrating the equilibrated model described above for a further 20 yr, during which the linear sensitivities are computed at every grid point and time step via algorithmic differentiation using the commercial tool Transformation of Algorithms in Fortran (TAF; <http://www.fastopt.com/>; Giering and Kaminski 1998). Because of seasonal variability in the equilibrated model, 12 adjoint experiments are required to fully probe the sensitivity of AMOC<sub>25N</sub>. Each experiment is identical except that the sensitivity calculation is performed for the January-mean AMOC<sub>25N</sub> through to the December-mean AMOC<sub>25N</sub> [ $\bar{\psi}^{\text{month}} = \bar{\psi}^{\text{jan}}, \bar{\psi}^{\text{feb}}, \dots, \bar{\psi}^{\text{dec}}$  in Eq. (3)]. To avoid repetition, the reader is referred to Pillar et al. (2016) for presentation of the time-evolving sensitivity distributions and discussion of the associated oceanic adjustment mechanisms. To briefly summarize the results of our earlier study, we note that AMOC<sub>25N</sub> possesses a short memory to fluctuations in surface wind forcing. Sensitivity maps reveal that AMOC<sub>25N</sub> mainly responds to fluctuations in the wind across  $25^\circ\text{N}$  and in the local upstream coastal waveguides, due to adjustments on monthly time scales. In contrast, AMOC<sub>25N</sub> possesses significant multidecadal memory of fluctuations in surface buoyancy forcing. Sensitivity maps reveal long baroclinic pathways linking AMOC<sub>25N</sub> to surface heat and buoyancy fluxes over the North Atlantic subpolar gyre. These results support the findings of earlier independent sensitivity studies (Czeschel et al. 2010; Heimbach et al. 2011). As first noted by Czeschel et al. (2010), modeled AMOC<sub>25N</sub> sensitivity to high-latitude buoyancy fluxes oscillates on decadal time scales. This is consistent with the existence of oscillatory modes of decadal variability in many independent OGCMs (e.g., Frankcombe et al. 2010), although the extent to which these modes depend on surface restoring is unclear. Our results are also consistent with published studies indicating that variability in the subtropical AMOC is dominated by wind forcing on subannual time scales (e.g., Biastoch et al. 2008; Zhao and Johns 2014; Polo et al. 2014) and by thermal forcing on time scales of a decade and longer (e.g., Delworth and Mann 2000; Eden and Willebrand 2001; Yeager and Danabasoglu 2014).

Linearization of the AMOC<sub>25N</sub> sensitivity calculation restricts our consideration to small-amplitude perturbations in the surface fluxes, acting over a finite time period. At the model resolution used in this study, the adjoint has been found to reliably approximate the full (nonlinear) response of the large-scale circulation to typical variations in the surface forcing for  $\sim 15$  yr (Czeschel et al. 2010; Heimbach et al. 2011; Zanna et al. 2012). This is easily sufficient for understanding the

TABLE 1. Overview of the air–sea flux products compared in this study. For all products, we use monthly values of air–sea flux. Approximate resolution in degrees is given for spectral models.

Product	Short name	Time period	Grid resolution	Reference
NCEP–NCAR Reanalysis I	NCEPI	Jan 1948–Jan 2015	2° × 2° × 28 levels	Kalnay et al. (1996)
NCEP–DOE AMIP-II reanalysis	NCEPII	Jan 1979–Jul 2015	2° × 2° × 28 levels	Kanamitsu et al. (2002)
ERA-Interim reanalysis	ERA-INT	Jan 1979–Mar 2015	0.75° × 0.75° × 60 levels	Dee et al. (2011)
Japanese 55-year Reanalysis	JRA55	Jan 1958–Dec 2012	0.6° × 0.6° × 60 levels	Kobayashi et al. (2015)
NOAA–CIRES Twentieth Century Reanalysis	20CR	Jan 1851–Dec 2011	2° × 2° × 28 levels	Compo et al. (2011)

observed annual cycle in the Florida Straits component of the AMOC, which is dominated by wind-driven barotropic adjustments on time scales of 1 month (Czeschel et al. 2012). However, it is too short to fully explore observed lower-frequency variations in the basinwide meridional volume transport, which is influenced by buoyancy-driven baroclinic adjustment on multidecadal time scales (see review by Buckley and Marshall 2016, and references therein). In section 4 of this paper, we construct time series of externally forced  $AMOC_{25N}$  variations using the maximum (15 yr) response history available using the adjoint. Although these time series are unequillibrated, we can provide a meaningful assessment of the  $AMOC_{25N}$  uncertainty generated by forcing uncertainty applied on a 15-yr time scale, which we show to be significant. We will return to discuss this later.

### c. Reanalysis ensemble

Monthly mean air–sea fluxes of heat, freshwater, zonal momentum, and meridional momentum are selected from five widely used atmospheric reanalysis products: the ERA-Interim reanalysis (ERA-INT), NCEP–NCAR Reanalysis-I (NCEPI), NCEPII, the Japanese 55-year Reanalysis (JRA55), and the 20CR. Temporal coverage, spatial resolution, and key references for these products are given in Table 1. All five products provide air–sea flux estimates for the common period January 1979–December 2011.

### d. $AMOC_{25N}$ response calculation

Air–sea fluxes from each of the five selected products,  $F_i$ , are first interpolated onto the MITgcm  $1^\circ \times 1^\circ$  model grid. Monthly flux anomalies,  $\Delta F_i$ , about the climatological seasonal cycle,  $F_i^{sc}$ , are then computed as

$$\Delta F_i = F_i - F_i^{sc}, \quad (1)$$

where for each product  $i$ , of length  $n$  months,  $\Delta F_i$  is an  $n$ -month time series at each grid point. At each grid point  $F_i^{sc}$  is an  $n$ -month time series, repeating itself every

12 months. The flux anomalies computed in Eq. (1) are projected onto the model-based patterns of  $AMOC_{25N}$  linear sensitivity to the corresponding flux,  $\partial\bar{\psi}^{\text{month}}/\partial F$ . Integrating across the globe, accumulating over forcing lead time  $T_{\text{lead}}$ , and convolving the reconstructions for all 12 months (Pillar 2013) yields time series of monthly wind-driven and buoyancy-driven  $AMOC_{25N}$  variations,  $\Delta\bar{\psi}_i$ :

$$\Delta\bar{\psi}_i(t) = \sum_{T_{\text{lead}}=1 \text{ month}}^{15 \text{ years}} \iint \frac{\partial\bar{\psi}}{\partial F} \Delta F_i dx dy. \quad (2)$$

Note that  $\Delta\bar{\psi}_i(t)$  is a time series of perturbations of the monthly mean transport about the seasonal cycle in the steady-state model integration (section 3a). We derive five time series for comparison; one for each reanalysis product ( $i = 1:5$ ). In Eq. (2) we sum over the full 15-yr response history that is reliably approximated by the adjoint. Estimates of  $AMOC_{25N}$  variability accounting for this 15-yr response history can be made for the period January 1994–December 2011 for all five reanalysis products.

The real power of adjoint-based attribution lies in the fact that the full space and time structure of  $AMOC_{25N}$  adjustment is contained within the linearized sensitivities,  $\partial\bar{\psi}^{\text{month}}/\partial F(x, y, T_{\text{lead}})$ . These sensitivities give the  $AMOC_{25N}$  anomaly, in any given month of the year, that would result from a unit anomaly in air–sea flux  $F$ , occurring at location  $(x, y)$  and lead time-interval  $T_{\text{lead}}$  [see Pillar et al. (2016) for maps and worked examples]. By examining the unintegrated projection,

$$\begin{aligned} \Delta\bar{\psi}_i^{\text{month}}(x, y, t, T_{\text{lead}}, F) \\ = \frac{\partial\bar{\psi}^{\text{month}}}{\partial F}(x, y, T_{\text{lead}}) \Delta F_i(x, y, t - T_{\text{lead}}), \end{aligned} \quad (3)$$

we determine the space–time origins of  $AMOC_{25N}$  anomalies (and  $AMOC_{25N}$  uncertainty). Here,  $\Delta\bar{\psi}_i^{\text{month}}$  is the  $AMOC_{25N}$  anomaly at time  $t$ , forced by anomalies in air–sea flux  $F$ . These flux anomalies,  $\Delta F_i(x, y, t - T_{\text{lead}})$ , occur at location  $(x, y)$  at the earlier time  $t - T_{\text{lead}}$  and are

derived from reanalysis product  $i$ . Note that we assume the sensitivities are date invariant, so that they depend on the lead interval,  $T_{\text{lead}}$ , of the forcing but not the time,  $t$ , at which the  $\text{AMOC}_{25\text{N}}$  anomaly occurs. Although  $\text{AMOC}_{25\text{N}}$  adjustment mechanisms do depend on the background climate state, we consider that background changes are small on the time scales considered below. This assumption is supported by the presence of only weak low-frequency  $\text{AMOC}_{25\text{N}}$  variability in our model.

#### 4. Results

We now compute the impact of air–sea flux uncertainty on  $\text{AMOC}_{25\text{N}}$  variations about the modeled seasonal cycle. We start by presenting the net impact of forcing uncertainty, applied over a 15-yr time scale, on the  $\text{AMOC}_{25\text{N}}$  anomaly time series computed using Eq. (2). We then use the full space–time adjustment history provided by the adjoint to explore where, and at what lead time, the air–sea flux uncertainty drives the largest uncertainty in  $\text{AMOC}_{25\text{N}}$  fluctuations about the seasonal cycle [Eq. (3)]. Throughout the paper,  $\text{AMOC}_{25\text{N}}$  uncertainty is defined as the range in the  $\text{AMOC}_{25\text{N}}$  anomaly estimates across the five-member ensemble.

##### *a. Impact of reanalysis uncertainty on $\text{AMOC}_{25\text{N}}$*

Time series of monthly variability in  $\text{AMOC}_{25\text{N}}$  from 1960 to 2017 due to interannual anomalies in zonal wind stress, meridional wind stress, surface heat fluxes, and surface freshwater fluxes [Eq. (2)] are shown in Fig. 1 for all five members of the reanalysis ensemble. For all reanalysis members, wind forcing dominates the high-frequency variations in  $\text{AMOC}_{25\text{N}}$ , with good agreement across the ensemble in the occurrence of high-amplitude excursions exceeding 5 Sv, driven by zonal wind forcing (Fig. 1a). Events analogous to the extreme winter minima observed in 2009/10 and 2013 across the RAPID array (e.g., McCarthy et al. 2012; Smeed et al. 2014) occur approximately once per decade (Fig. 1e). Decomposing the zonal-wind-driven  $\text{AMOC}_{25\text{N}}$  variability (Fig. 1a) into instantaneous Ekman and residual (total–Ekman) components [as shown for the NCEPII-based estimate in Pillar et al. (2016)] reveals that these extreme events are primarily anomalous Ekman transports [in agreement with Blaker et al. (2015)]. These “extremes” are captured in all five reanalysis products and occur at a rate consistent with our expectations for a Gaussian process (Wunsch and Heimbach 2013b).

For all reanalysis members, buoyancy forcing dominates the decadal variability of  $\text{AMOC}_{25\text{N}}$ , consistent with previous reanalysis-forced OGCM studies by

Biastoch et al. (2008) and Yeager and Danabasoglu (2014). Across the ensemble, there is agreement in the steady weakening of  $\text{AMOC}_{25\text{N}}$  between 1995 and 2003 and subsequent recovery toward 2009 (Fig. 1e), dominated by surface heat fluxes (Fig. 1c). Interestingly, at the time of reversal of this multiannual trend, a more regular seasonal cycle is visible in the heat-driven  $\text{AMOC}_{25\text{N}}$ . This cycle has a peak-to-peak amplitude of approximately 1 Sv and persists between 2003 and 2006 for all reanalysis products (Fig. 1c). Agreement in the timing of low-frequency variations in  $\text{AMOC}_{25\text{N}}$  driven by surface freshwater fluxes can also be seen across the ensemble, except for the periods 1977–82 and 2008–12 for the 20CR reconstruction (Fig. 1d).

Although there is some coherence in the timing of low-frequency trends in  $\text{AMOC}_{25\text{N}}$  driven by surface buoyancy fluxes, there is notable uncertainty in the amplitude of the buoyancy-driven  $\text{AMOC}_{25\text{N}}$  anomaly across the reanalysis ensemble (Figs. 1c,d). For example, for the decade 1969–79,  $\text{AMOC}_{25\text{N}}$  anomalies produced by 20CR surface heat fluxes are negative, while those produced by NCEPI surface heat fluxes are positive. For the period 2003–15,  $\text{AMOC}_{25\text{N}}$  anomalies produced by NCEPI and NCEPII surface freshwater fluxes are negative, while those produced by ERA-INT are positive.

The time-average (for the period 1994–2011) ensemble ranges in  $\text{AMOC}_{25\text{N}}$  forced by zonal and meridional wind stress uncertainties are 0.7 and 0.4 Sv, respectively (Figs. 1a,b). Interestingly, the time-averaged  $\text{AMOC}_{25\text{N}}$  range due to the total zonal wind forcing is smaller than the 1.1-Sv uncertainty associated with the Ekman component alone (not shown). Uncertainty in surface heat and freshwater fluxes across the ensemble produce time-averaged ranges of 1.8 and 0.8 Sv in  $\text{AMOC}_{25\text{N}}$ , respectively (Figs. 1c,d). The ensemble range in the total  $\text{AMOC}_{25\text{N}}$  is consistently less than the range of the individual buoyancy and momentum-driven components combined. The time-averaged ensemble range in the total  $\text{AMOC}_{25\text{N}}$  is 2.1 Sv. In any given month, it can be as large as 5.6 Sv, dominated by surface heat flux uncertainty (Fig. 1e).

As discussed in section 3b, the computed buoyancy-driven  $\text{AMOC}_{25\text{N}}$  is unequilibrated, meaning that the time series shown in Fig. 1e do not provide reliable estimates of variability in the basinwide meridional volume transport that would have been observed across 25°N at the date shown along the  $x$  axis (Pillar et al. 2016). Notably, in our unconverged  $\text{AMOC}_{25\text{N}}$  estimate, we simulate a gradual strengthening of  $\text{AMOC}_{25\text{N}}$  through the second half of the 1980s, inconsistent with the sustained strengthening from 1980 through to the mid-1990s simulated in numerous modeling studies (e.g., Eden and Willebrand 2001; Bentsen et al. 2004; Böning

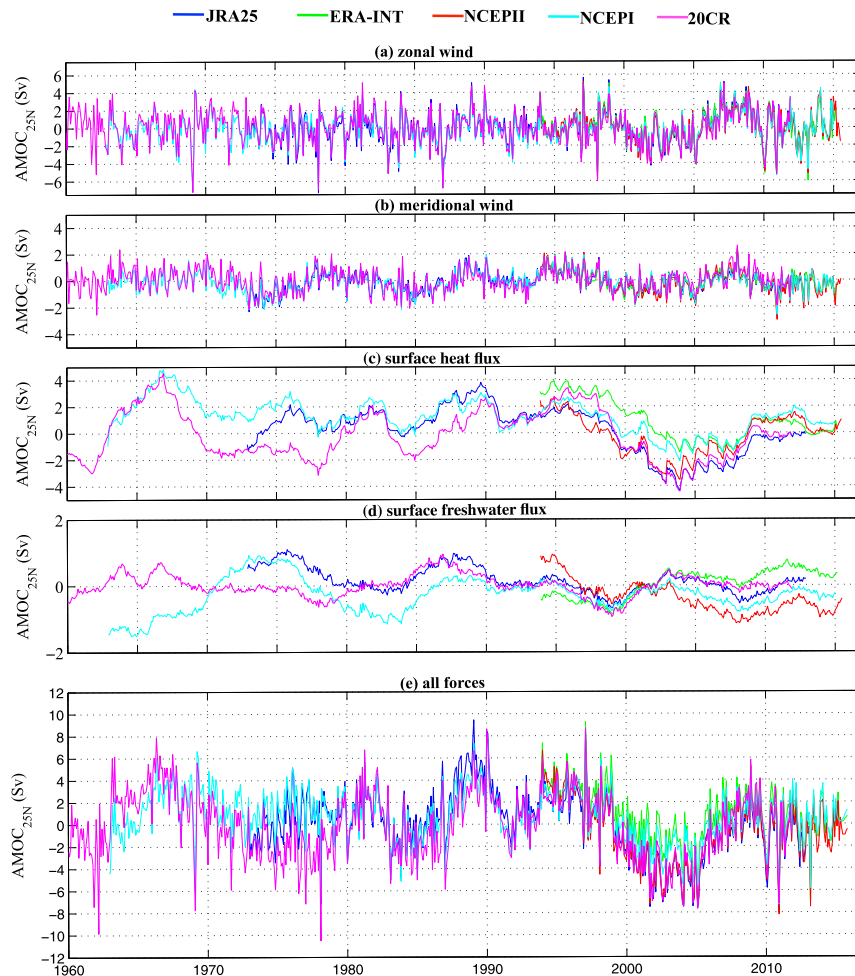


FIG. 1.  $AMOC_{25N}$  variability generated by interannual anomalies in (a) zonal wind stress, (b) meridional wind stress, (c) surface heat flux, (d) surface freshwater flux, and (e) all forcing [produced by combining (a)–(d)] for the period January 1960–January 2016. These time series are computed by convolving model-derived patterns of linear sensitivity of  $AMOC_{25N}$  to air–sea fluxes with corresponding forcing anomalies from reanalysis [Eq. (1)], integrating in space and accumulating in time over a 15-yr response history [Eq. (2)]. Colors indicate the reanalysis product providing the surface forcing anomalies (see legend and Table 1). An  $AMOC_{25N}$  estimate constructed from a 15-yr response history is available for all five reanalysis members for the period January 1994–December 2011. Note that the y-axis limits are not the same for (a)–(e).

2006; Robson et al. 2012a; Yeager et al. 2015), including the COREv2-forced hindcast ensemble (Danabasoglu et al. 2016). We also estimate a sustained strengthening of  $AMOC_{25N}$  through most of the decade 2000–10, when observations and ocean reanalyses support a weakening trend from 2005 (Jackson et al. 2016) and ocean state estimates suggest a statistically steady state persisting throughout the 1990s and 2000s (Wunsch and Heimbach 2013b).

Although we cannot estimate the equilibrated response of  $AMOC_{25N}$  to uncertain air–sea fluxes, we can examine the first 15 yr of  $AMOC_{25N}$  adjustment. This

time scale is more relevant for decadal prediction efforts than the multicentennial-to-millennial  $AMOC$  equilibration time scale. Figure 1 illustrates that after only 15 yr the amplitude of the uncertainty in  $AMOC_{25N}$  generated by forcing uncertainty is comparable to the amplitude of  $AMOC_{25N}$  variations, meriting further investigation. We now seek to determine how this uncertainty evolves.

#### b. Time origins of reanalysis uncertainty impact

Figure 1 highlights key times at which our ensemble of  $AMOC_{25N}$  variability estimates diverge, but it is not yet

clear exactly when in the response history this divergence is generated. For example, the  $\sim 3$ -Sv ensemble spread occurring in 2002 (Fig. 1e) is due principally to uncertainty in the thermally driven component (Fig. 1c). The thermally driven component is integrated over a 15-yr response history [Eq. (2)], so the  $\sim 3$ -Sv spread in 2002 is the accumulated response to reanalysis heat flux uncertainties between 1988 and 2002. We now seek to determine when uncertainty in reanalysis surface forcing is most potent in driving uncertainty in model-based estimates of AMOC<sub>25N</sub> variability.

In Fig. 2 we show how the spatially integrated response to each forcing accumulates through time for each reanalysis product. Panels showing AMOC<sub>25N</sub> anomalies driven by NCEP-II fluxes (Figs. 2d,j,p,v) are Hovmöller representations of the time series presented in Fig. 2 of Pillar et al. (2016). The individual contribution of each month of forcing to the AMOC<sub>25N</sub> anomaly is shown in Fig. 3.

There are many comparable features across the reanalysis ensemble and the reader is referred to the description of the NCEP-II-based estimate in Pillar et al. (2016) for a full discussion. In summary, all transport estimates are characterized by the dominance of fast barotropic and slow baroclinic adjustments in setting the wind-driven and buoyancy-driven responses, respectively. An interesting feature of the response not noted in Pillar et al. (2016) is the change in sign of the buoyancy-driven AMOC<sub>25N</sub> anomaly between consecutive forcing months and for the same forcing month with an increase in the AMOC<sub>25N</sub> lag considered (Figs. 2m–q and 2s–w and Figs. S2m–q and S2s–w in the online supplemental material for this paper). While the former is due to seasonality in the surface buoyancy fluxes, the latter is due to low-frequency changes in both the sign of the high-latitude buoyancy forcing and the sign of the AMOC<sub>25N</sub> sensitivity to high-latitude buoyancy fluxes (Czeschel et al. 2010). The impact of low-frequency changes in the sensitivity can be seen in Figs. 3m–q and 3s–w. Most notably, the ERA-INT, NCEP-I, and NCEP-II-based AMOC<sub>25N</sub> estimates show that the global surface freshwater fluxes in December 2001 drive a strengthening of AMOC<sub>25N</sub> from 2005 to mid-2011, but these same fluxes drive a weakening of the AMOC<sub>25N</sub> from mid-2011 through to 2016.

Despite many qualitative similarities in the AMOC<sub>25N</sub> response to air–sea fluxes across the reanalysis ensemble, the amplitude of the ensemble spread is comparable to the amplitude of the ensemble mean AMOC<sub>25N</sub> response and exhibits similar time origins (Figs. 2f,l,r,x and 3f,l,r,x). The time-mean evolution of AMOC<sub>25N</sub> spread as a function of lag from the causal forcing uncertainty is shown in Fig. 4. In general, the AMOC<sub>25N</sub> spread increases with

an increase in the maximum length of the response history considered (Figs. 4a–d), but with a rate dependent on the air–sea flux. The wind-driven AMOC<sub>25N</sub> spread is dominated by uncertainty in the recent wind field involved in the fast barotropic adjustments (Figs. 2f,l and 4a,b). These winds generate AMOC<sub>25N</sub> spreads with time means of approximately 0.5 and 0.4 Sv, respectively (Figs. 4a,b), which for some months are as large as 1.7 and 1.2 Sv (Figs. 3f,l). However, they lose potency rapidly; at lags of a year or longer, the monthly AMOC<sub>25N</sub> response to the same forcing uncertainty is only 0.02 Sv on average (Figs. 4e,f), and never exceeds 0.2 Sv in any month (Figs. 3f,l), for both zonal and meridional wind-driven spreads. Returning to consider the AMOC<sub>25N</sub> variability estimate constructed using the full 15-yr response history accessible using the adjoint (Fig. 1), we can now deduce from Figs. 4a,b that uncertainty in the concurrent (AMOC<sub>25N</sub> lag = 1 month) wind field typically accounts for 70% of the total wind-induced uncertainty in AMOC<sub>25N</sub> at any date.

In contrast, the buoyancy-driven AMOC<sub>25N</sub> spread accumulates gradually with lag from the causal forcing uncertainty (Figs. 2r,x and 4c,d), through slower baroclinic adjustments. This is true for both the heat-flux-driven and freshwater-flux-driven spreads, despite a notable barotropic adjustment to surface freshwater uncertainties (Figs. 3x and 4h). On average, heat forcing uncertainties become most potent at lags of approximately 7 yr, generating an AMOC<sub>25N</sub> spread with a time mean of approximately 0.07 Sv (Fig. 4g), but for some months it is as large as 0.3 Sv (Fig. 3r). Following the initial barotropic response, the freshwater-flux-driven AMOC<sub>25N</sub> spread achieves a secondary maximum after approximately 11 yr, generating an AMOC<sub>25N</sub> spread with a time mean of approximately 0.02 Sv (Fig. 4h), and never exceeding 0.07 Sv (Fig. 3x). Returning to consider the AMOC<sub>25N</sub> variability estimate constructed using the full 15-yr response history accessible using the adjoint (Fig. 1), we can now deduce from Figs. 4c,d that on average we only account for 70% of the total buoyancy-induced AMOC<sub>25N</sub> uncertainty at any date if we consider all uncertainty in the reanalyzed buoyancy field over the previous 10 yr.

To determine the relative importance of wind and buoyancy forcing uncertainties, we plot the fractional contribution of each air–sea flux to the total AMOC<sub>25N</sub> uncertainty in Fig. 5. We examine both the cumulative impact of all prior forcing uncertainty (solid lines) and the impact of forcing uncertainty in a single month (dashed lines) on AMOC<sub>25N</sub> at the lag shown along the  $x$  axis. In general, wind stress uncertainties become less important with increasing AMOC<sub>25N</sub> lag, while buoyancy uncertainties become relatively more important. On



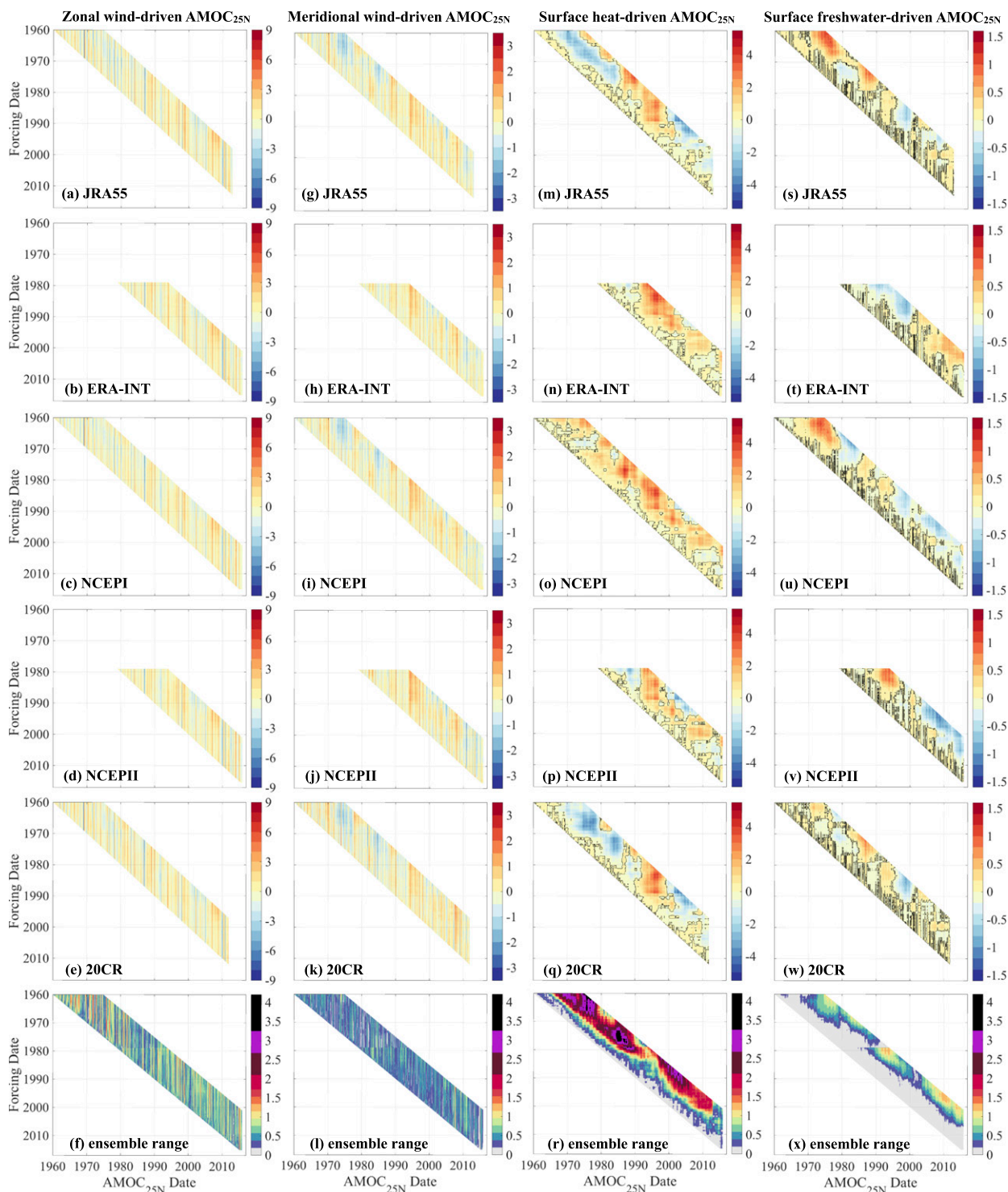


FIG. 2. Time origins of  $AMOC_{25N}$  variability (Sv) driven by (a)–(e) zonal wind stress, (g)–(k) meridional wind stress, (m)–(q) surface heat fluxes, and (s)–(w) surface freshwater fluxes taken from (a),(g),(m),(s) JRA55; (b),(h),(n),(t) ERA-INT; (c),(i),(o),(u) NCEPI; (d),(j),(p),(v) NCEPII; and (e),(k),(q),(w) 20CR reanalyses. Note that at each date shown along the x axis,  $AMOC_{25N}$  is calculated as the accumulated response to all past forcing up to the date shown along the y axis, following Eq. (2). A maximum forcing lead time of 15 yr is considered; the associated time series is shown in Fig. 1. NCEPII panels are Hovmöller representations of the time series shown in Fig. 2 of Pillar et al. (2016). The 0-Sv contour is shown in black for the buoyancy-driven  $AMOC_{25N}$  [(m)–(q) and (s)–(w)]. The reanalysis ensemble range in the cumulative response (Sv) is shown in the bottom row for  $AMOC_{25N}$  variations driven by reanalyses of the (f) zonal wind, (l) meridional wind, (r) surface heat fluxes, and (x) surface freshwater fluxes. The reader is referred to Fig. S1 in the online supplemental material for an alternative version of this figure plotted in  $AMOC_{25N}$  date–forcing lead time space, in which details of the response shown here are easier to see.

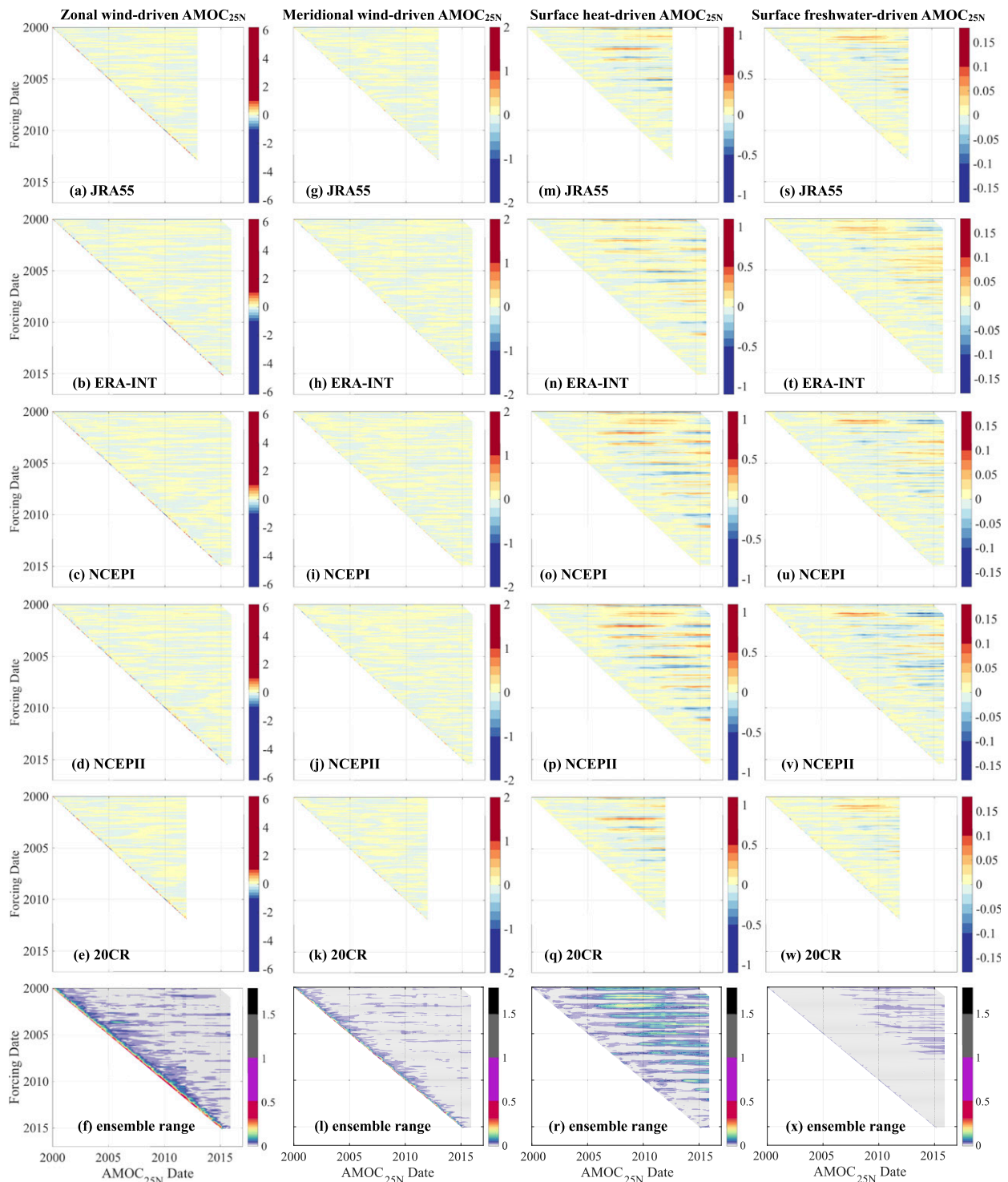


FIG. 3. As in Fig. 2, but showing the separate contribution of each month of forcing (at the date shown along the y axis) to  $AMOC_{25N}$  (Sv) (at the date shown along the x axis) for each member of the reanalysis ensemble. By integrating along the y axis we would recover Fig. 2. Here, we show only the  $AMOC_{25N}$  forced by air–sea fluxes from the year 2000 onward, allowing characteristics of the  $AMOC_{25N}$  response—shared by the full time series—to be more easily visualized. For example, it can be seen that the largest (a)–(e) and (g)–(k) wind-driven  $AMOC_{25N}$  variability and (f) and (l) wind-driven  $AMOC_{25N}$  uncertainties occur at very short lags and do not appear to show a strong seasonal dependency. In contrast, the largest (m)–(q) heat-flux-driven  $AMOC_{25N}$  variability and (r) heat-flux-driven  $AMOC_{25N}$  uncertainties occur at lags exceeding 5 yr and show strong seasonality. The reader is referred to Fig. S2 in the online supplemental material for an alternative version of this figure plotted in  $AMOC_{25N}$  date–forcing lead time space, in which details of the response shown here are easier to see.

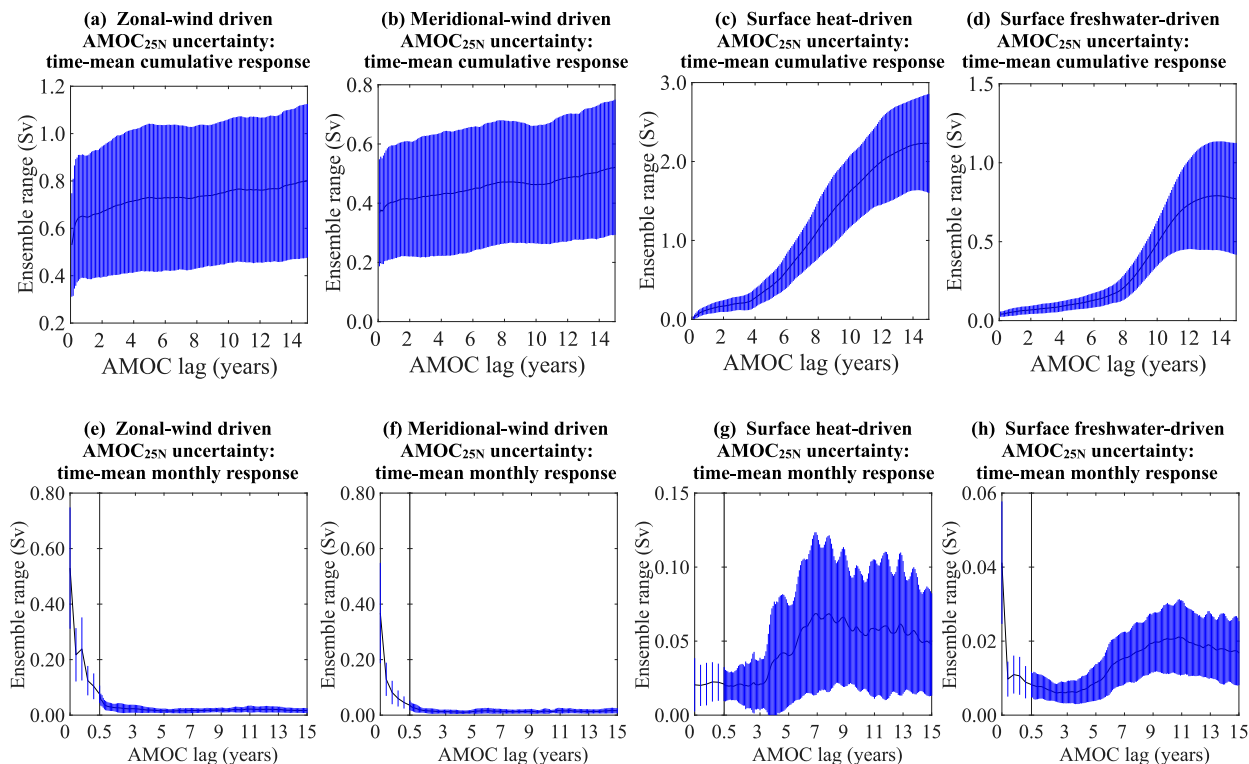


FIG. 4. The solid line shows the time-mean evolution of  $AMOC_{25N}$  uncertainty as a function of time lag from the causal forcing uncertainty in (a),(e) zonal wind stress, (b),(f) meridional wind stress, (c),(g) surface heat fluxes, and (d),(h) surface freshwater fluxes. This evolution is shown for both (a)–(d) the cumulative response to all forcing leading up until the  $AMOC_{25N}$  lag shown along the x axis (see Figs. 2f, 1, r, x) and (e)–(h) the response to 1 month of forcing at the exact  $AMOC_{25N}$  lag shown along the x axis (see Figs. 3f, 1, r, x). The time mean is computed for the period January 1994–December 2011, when an  $AMOC_{25N}$  estimate constructed from a 15-yr response history can be obtained from all five reanalysis members. The standard deviation is shaded to illustrate that, qualitatively, the evolution of  $AMOC_{25N}$  uncertainty is not date dependent. Note that the y-axis limits are not the same for (a)–(h). The x axis has been stretched in (e)–(h) to resolve initial barotropic adjustments. The key result is that in (e),(f) wind stress uncertainties are most potent at short lags and have very little impact on  $AMOC_{25N}$  uncertainty at lags exceeding a year. Therefore, even if we consider a 15-yr forcing history, the (a),(b) total wind-driven  $AMOC_{25N}$  uncertainty is dominated by uncertainty in recent wind stress. Although (h) freshwater flux uncertainties drive a large instantaneous  $AMOC_{25N}$  response, they have a sustained impact on  $AMOC_{25N}$  uncertainty only at lags exceeding 4 years. Similarly (g) surface heat flux uncertainties have little effect at short lag and are most potent at a lag of 7 yr. As a result, (c),(d) total buoyancy-driven  $AMOC_{25N}$  uncertainty is small at short lags, increasing almost monotonically as a longer forcing history is taken into account.

average, wind stress uncertainty is responsible for 94% of the instantly generated  $AMOC_{25N}$  spread; 55% arises from zonal-wind uncertainty alone. For lags of up to 6.5 yr, the cumulative  $AMOC_{25N}$  response to prior forcing uncertainty is dominated by uncertainty in the zonal wind (Fig. 5, solid lines). At longer lags, surface heat flux uncertainty is dominant. By a lag of 15 yr, surface heat flux uncertainty is responsible for 52% of the cumulative  $AMOC_{25N}$  response to prior forcing uncertainty; uncertainties in the zonal-wind stress, surface freshwater flux, and meridional-wind stress are responsible for 18%, 18%, and 12% of the total  $AMOC_{25N}$  spread, respectively.

The unaccumulated uncertainties (Fig. 5, dashed lines) show similar behavior to the accumulated uncertainties (Fig. 5, solid lines) described above. However, the heat flux

uncertainties dominate the unaccumulated  $AMOC_{25N}$  spread after a lag of only 3.3 yr, due to the rapid loss of  $AMOC_{25N}$  memory to past wind stress perturbations.

### c. Seasonality of reanalysis uncertainty impact

An additional feature of the  $AMOC_{25N}$  variability time series that is consistent across the reanalysis ensemble is the strong seasonality in the  $AMOC_{25N}$  response to buoyancy forcing (Figs. 3m–q and 3s–w). To investigate this further, we sort the  $AMOC_{25N}$  response by the month of causal forcing. The absolute  $AMOC_{25N}$  variations driven by air–sea fluxes in each of the 12 months of the year, for each reanalysis product, are then averaged for all years common to the  $AMOC_{25N}$  ensemble (January 1994–December 2011), and plotted as a function of forcing lead time in Fig. 6.

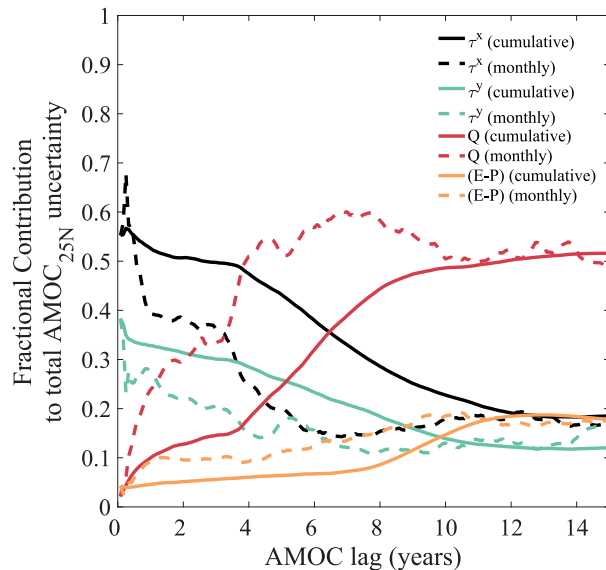


FIG. 5. Fractional contribution of uncertainty in reanalyses of zonal wind stress (black), meridional wind stress (green), surface heat flux (red), and surface freshwater flux (orange), to the total uncertainty in the modeled  $AMOC_{25N}$ . We show the fractional contributions to both the cumulative response to all forcing uncertainty leading up until the  $AMOC_{25N}$  lag shown along the  $x$  axis (solid lines) and the response to forcing at the  $AMOC_{25N}$  lag shown along the  $x$  axis (dashed lines). The fractional contributions are computed from the time-mean uncertainties shown in Fig. 4. The time mean is computed for the period January 1994–December 2011, when an  $AMOC_{25N}$  estimate constructed from a 15-yr response history can be obtained from all five reanalysis members. The key result is that zonal wind uncertainties dominate the total externally forced  $AMOC_{25N}$  uncertainty at lags of up to 6.5 yr (solid black) and surface heat flux uncertainties dominate at longer lags (solid red).

For all reanalyses, seasonality in the heat-flux-driven  $AMOC_{25N}$  is most notable (Fig. 6c). For almost all lags considered, the largest-amplitude monthly anomalies in the heat-flux-driven  $AMOC_{25N}$  occur as a result of flux anomalies during February; the smallest heat-flux-driven  $AMOC_{25N}$  anomalies occur as a result of flux anomalies during July. For lags of around 7 and 13 yr, seasonality in the  $AMOC_{25N}$  sensitivity to surface heat fluxes is largest and the  $AMOC_{25N}$  response shown in Fig. 6c can differ by up to 0.35 Sv, depending on whether the heat flux anomalies occurred in early spring or during summer of the same year. Seasonality in the potency of surface freshwater fluxes has an amplitude that is an order of magnitude smaller than the seasonality in the potency of the surface heat fluxes, but has the same timing (Figs. 6d), as a result of the similar sensitivity of  $AMOC_{25N}$  to changes in surface freshwater and heat (Pillar et al. 2016).

For all reanalyses, the seasonality of the instantaneous  $AMOC_{25N}$  response to wind stress has the same timing

as the buoyancy-driven response at longer lags described above. However, with increasing  $AMOC_{25N}$  lag, the seasonal potency of the surface wind stress anomalies varies in a more complex manner (Figs. 6a,b). Slow wind-driven adjustment of  $AMOC_{25N}$  on time scales approaching 15 yr is largely dominated by wind anomalies that occurred in October and November; wind anomalies that occurred in April–July drive the smallest-amplitude response (Figs. 6a,b).

The generation of  $AMOC_{25N}$  spread by reanalysis forcing uncertainty also exhibits a strong seasonality (Figs. 3f,l,r,x). If the seasonality is set by ocean dynamics [i.e., contained within the linear sensitivity patterns used in Eq. (3)], as opposed to the forcing uncertainty [i.e., differences in  $\Delta F_i$  used in Eq. (3)], we expect the transport uncertainty to have the same seasonality as the transport (Fig. 6). This is true for the buoyancy-forced response; at almost all lags, the largest  $AMOC_{25N}$  spread is generated by February heat flux uncertainties, while June–September heat flux uncertainties have a vanishingly small impact on  $AMOC_{25N}$  (Fig. 7c, consistent with the seasonal potency of the heat flux forcing described above and shown in Fig. 6c). On average, at any lag, 17% of the total heat-flux-driven  $AMOC_{25N}$  spread is due to February heat flux uncertainties, exceeding the 13% driven by June–September heat flux uncertainties combined.

The seasonalities of the wind-driven  $AMOC_{25N}$  (Figs. 6a,b) and the wind-driven  $AMOC_{25N}$  spread (Figs. 7a,b) are different, suggesting seasonality in the forcing uncertainty may play a role. Let us focus on the  $AMOC_{25N}$  response at lag = 0, when the wind stress uncertainty has the largest impact on  $AMOC_{25N}$  (Fig. 5). Zonal-wind stress is most potent in January–February and generates the weakest instantaneous  $AMOC_{25N}$  response in July–September (Fig. 6a). However, zonal-wind stress uncertainties are most potent in September and have the weakest impact on the instantaneous  $AMOC_{25N}$  response in May (Fig. 7a). On average, 11% of the total wind-driven  $AMOC_{25N}$  spread is due to September wind stress uncertainties alone.

To better understand the time origins of  $AMOC_{25N}$  variability and  $AMOC_{25N}$  uncertainty (ensemble spread), we now turn to their spatial origins. By assessing where the forcing and forcing uncertainty are most potent, we will also be able to offer direction for targeted reductions of forcing uncertainty to improve skill in modeling  $AMOC_{25N}$ , which can also be applied to forecasting efforts.

#### d. Spatial origins of reanalysis uncertainty impact

We start by examining the spatial origins of  $AMOC_{25N}$  variability shown in Fig. 1, for the period when  $AMOC_{25N}$  estimates with  $T_{lag} = 15$  yr can be made

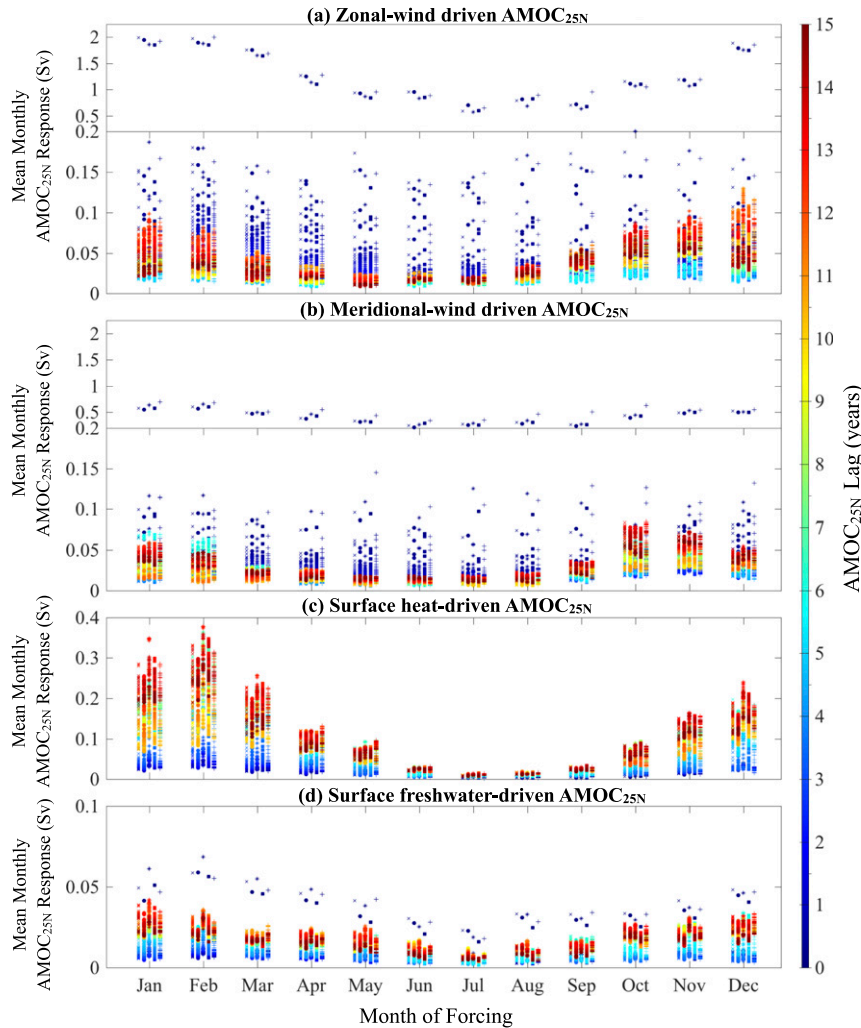


FIG. 6. Seasonal potency of reanalyses of global (a) zonal wind stress, (b) meridional wind stress, (c) surface heat fluxes, and (d) surface freshwater fluxes in generating  $AMOC_{25N}$  variations. Position along the  $x$  axis indicates the month of the year during which the forcing occurs. For each forcing month, five reanalysis ensemble members are shown: from left to right, JRA55 ( $\times$ ), ERA-INT ( $\bullet$ ), NCEP2 ( $\ast$ ), NCEP1 ( $\blacksquare$ ), and 20CR ( $+$ ). Color indicates the lag at which  $AMOC_{25N}$  responds to the imposed air–sea fluxes (or equivalently, the lead time of the forcing). We consider  $AMOC_{25N}$  lags from 1 month to 15 yr. For each reanalysis member, the  $AMOC_{25N}$  time series over the period common to the ensemble is considered. This common period varies with lag. For all reanalyses the  $AMOC_{25N}$  response at lag = 0 can be constructed for the period January 1979–December 2011; the  $AMOC_{25N}$  response at lag = 15 yr can be constructed for the period January 1994–December 2011. Position along the  $y$  axis indicates the time-mean amplitude of the absolute  $AMOC_{25N}$  anomaly. Consideration of the absolute  $AMOC_{25N}$  avoids cancellation in the time average. The key result is that the surface heat-flux-driven  $AMOC_{25N}$  variability in (c) is strongly seasonal; for almost all lags considered, the largest heat-flux-driven  $AMOC_{25N}$  occurs as a result of flux anomalies during February and the smallest heat-flux-driven  $AMOC_{25N}$  occurs as a result of flux anomalies during July. For all reanalyses, the seasonality of the instantaneous  $AMOC_{25N}$  response to wind stress has the same timing as the buoyancy-driven response at longer lags described above, but varies in a more complex manner with increasing lag.

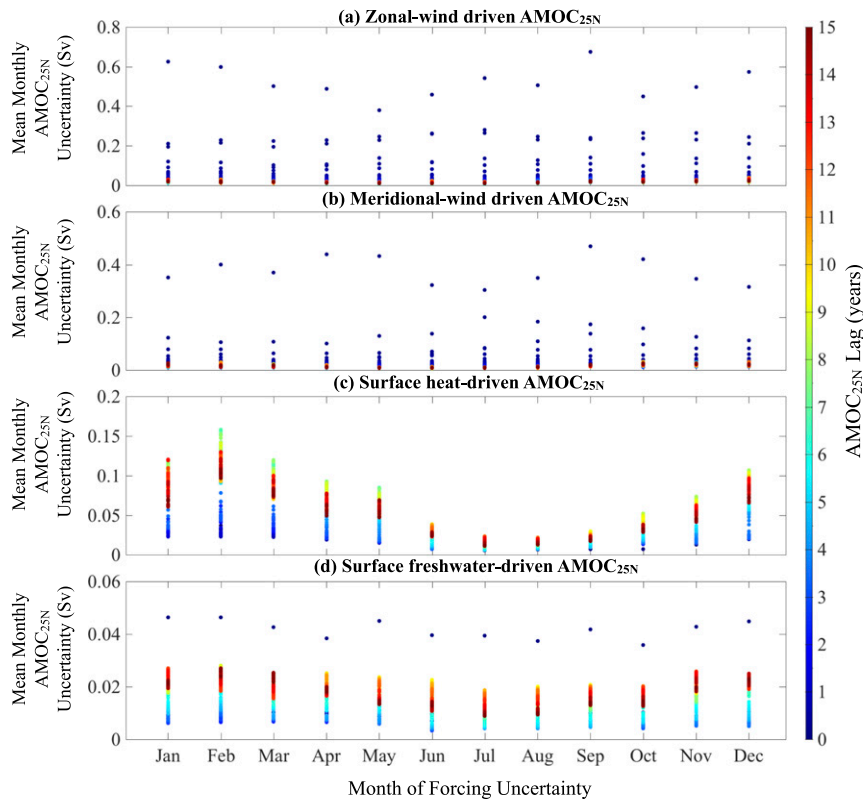


FIG. 7. Seasonal potency of uncertainty in reanalyses of global (a) zonal wind stress, (b) meridional wind stress, (c) surface heat fluxes, and (d) surface freshwater fluxes in generating uncertainty in  $AMOC_{25N}$ . The range is computed from the reanalysis ensemble members shown in Fig. 6. Position along the  $x$  axis indicates the month of the year in which the forcing uncertainty occurs. Color indicates the lag at which  $AMOC_{25N}$  responds to the air–sea flux uncertainty. The key result is that the heat-flux-driven  $AMOC_{25N}$  (Fig. 6c) and heat-flux-driven  $AMOC_{25N}$  uncertainty in (c) show similar seasonality. This suggests that ocean dynamics play a dominant role in setting the timing of the  $AMOC_{25N}$  response, as the seasonality is contained within the linear sensitivity patterns. In contrast, wind-driven  $AMOC_{25N}$  (Figs. 6a,b) and wind-driven  $AMOC_{25N}$  uncertainties in (a),(b) show different seasonality, suggesting seasonality in forcing uncertainty is important here.

with all reanalysis products (January 1994–December 2011). To avoid cancellation between the contributions to positive and negative  $AMOC_{25N}$  anomalies, we map the origins of the ensemble-mean time-integrated absolute  $AMOC_{25N}$  anomaly due to each air–sea flux in Fig. 8.<sup>1</sup> Significant generation of  $AMOC_{25N}$  variability is limited to air–sea fluxes over the Atlantic basin. Note that the amplitude of the time-integrated  $AMOC_{25N}$  anomalies shown in Fig. 8 depends on the temporal resolution (monthly) and spatial resolution ( $1^\circ \times 1^\circ$ ) of the projection [Eq. (2)] and is, therefore, somewhat

arbitrary. Both the date at which the  $AMOC_{25N}$  anomaly occurs and the lead time at which it was forced are masked by time integration, but can be deduced from Fig. 2.

On average,  $AMOC_{25N}$  variability is excited by zonal wind forcing in the vicinity of  $25^\circ N$  and throughout most of the North Atlantic basin (Fig. 8a). Of the total time-integrated zonal-wind-driven  $AMOC_{25N}$  variability, approximately one-quarter is excited by zonal winds within  $5^\circ$  of  $25^\circ N$  and one-quarter by zonal winds over the subpolar gyre (see Fig. 8 for integral areas). South of the equator, significant generation of  $AMOC_{25N}$  variability is limited to the vicinity of the Agulhas retroflexion. Reanalysis meridional wind most effectively generates  $AMOC_{25N}$  anomalies in the coastal waveguides upstream of  $25^\circ N$  (Fig. 8b), extending along the entire latitudinal span of the Atlantic basin for the 15-yr

<sup>1</sup> It is important here to recall that the  $AMOC_{25N}$  variability is computed about the modeled seasonal cycle in  $AMOC_{25N}$ ; forcing of the seasonal cycle in  $AMOC_{25N}$  by the seasonal cycle in forcing is not represented in Fig. 8.

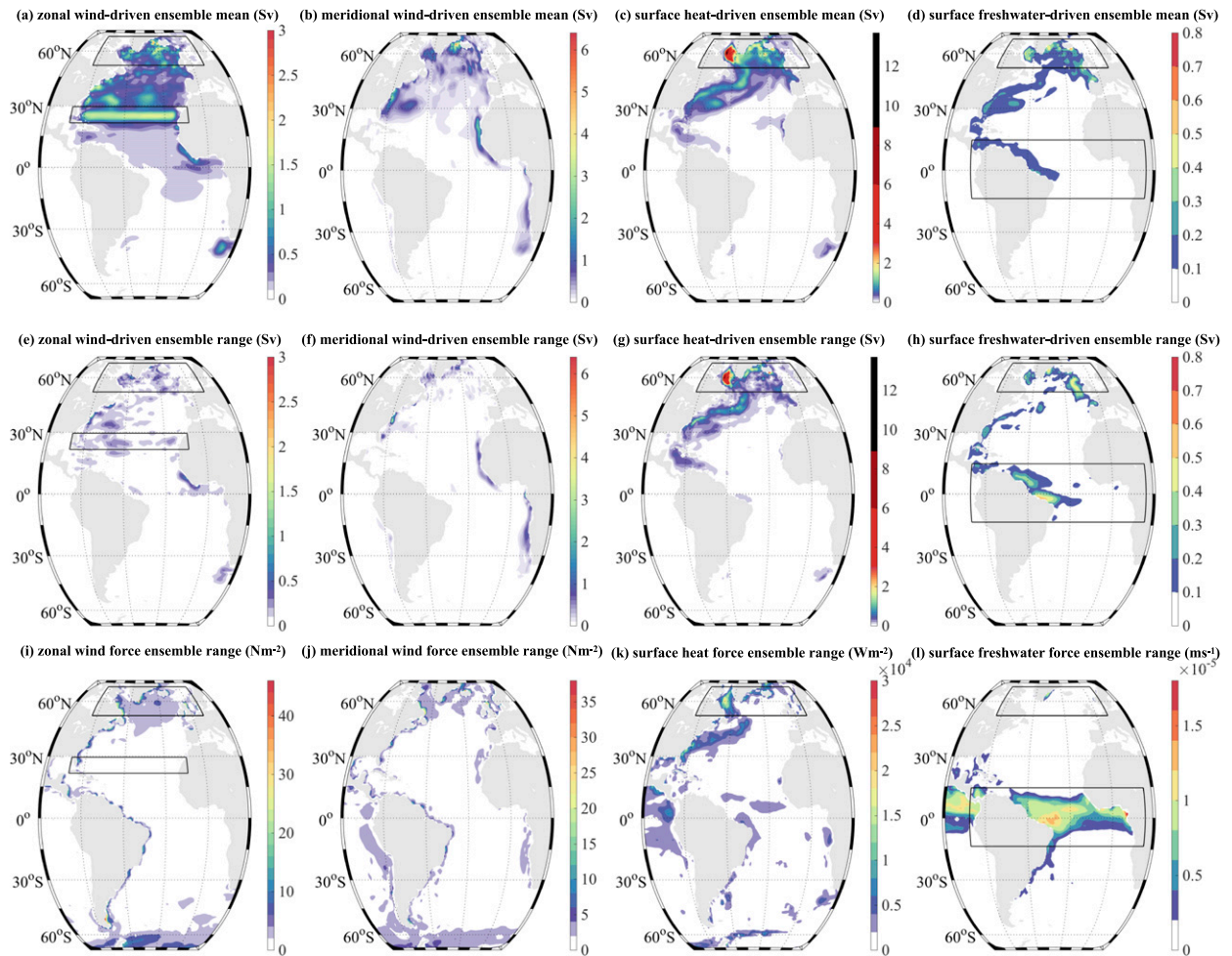


FIG. 8. Comparison of the spatial origins of (top) externally forced  $AMOC_{25N}$  variability with the origins of (middle) externally forced  $AMOC_{25N}$  uncertainty and (bottom) atmospheric forcing uncertainty. The aim is to determine whether key regions of (middle)  $AMOC_{25N}$  uncertainty generation are set by where the forcing is most uncertain (bottom row) or where the ocean is most sensitive to surface forcing anomalies (inferred from top row). Reanalysis ensemble-mean  $AMOC_{25N}$  anomalies (Sv) driven by (a) zonal wind, (b) meridional wind, (c) surface heat fluxes, and (d) surface freshwater fluxes, integrated over the period common to all reanalysis products shown in Fig. 1 (January 1994–December 2011). To avoid cancellation between contributions to positive and negative  $AMOC_{25N}$  anomalies, we map the time-integrated *absolute*  $AMOC_{25N}$  for this period. (e)–(h) As in (a)–(d), but showing the spatial origins of the time-integrated ensemble range in  $AMOC_{25N}$ . Grid cells contributing less than 0.1 Sv to the ensemble-mean  $AMOC_{25N}$  in (a)–(d) or ensemble-range in  $AMOC_{25N}$  in (e)–(h) over the entire period (January 1994–December 2011) are masked. The masked region includes the remainder of the global ocean (not shown). Spatial origins of the reanalysis ensemble range in absolute forcing from (i) zonal wind stress ( $N m^{-2}$ ), (j) meridional wind stress ( $N m^{-2}$ ), (k) surface heat fluxes ( $W m^{-2}$ ), and (l) surface freshwater fluxes ( $m s^{-1}$ ), integrated over the period January 1979–December 2011. The integration period is chosen to incorporate the full forcing history entailed in the  $AMOC_{25N}$  calculation for January 1994–December 2011. The *absolute* forcing is chosen to prevent cancellation between positive and negative fluxes in the time integral. Both of these choices enable comparison with (e)–(h). Black boxes delineate integral areas discussed in the text. Note that the amplitude of the time integrals in all panels depends on the temporal and spatial resolutions of the model configuration, the length of the time series considered in the integral, and the consideration of the absolute values, and is therefore somewhat arbitrary.

time scale considered here. A recent adjoint sensitivity study by Jones et al. (2018) has highlighted wind variability over the western African shelf as an important driver of heat content variability in the Labrador Sea. The reader is referred to their comprehensive discussion of the sequential adjustments connecting the western African shelf and Labrador Sea, allowing the eastern

boundary winds to impact North Atlantic Deep Water formation and overturning on subadvective time scales.

On average,  $AMOC_{25N}$  variability is excited by surface heat fluxes over the Gulf Stream, including the extension region, and throughout the North Atlantic subpolar ocean basin (Fig. 8c). Surface heat fluxes over the subpolar gyre excite approximately one-half of the

total time-integrated surface heat-flux-driven  $AMOC_{25N}$  variability. As for the zonal wind, reanalysis surface heat fluxes also drive significant  $AMOC_{25N}$  variability over the Agulhas retroflection. The  $AMOC_{25N}$  variability generated by reanalysis surface freshwater fluxes has similar spatial origins to that driven by surface heat fluxes, but extends farther south to include the western equatorial waveguides and is generally more strongly boundary intensified in the North Atlantic (Fig. 8d). Of the total time-integrated surface freshwater-driven  $AMOC_{25N}$  variability, approximately one-third is excited by freshwater fluxes over the subpolar gyre and one-fifth by freshwater fluxes in the tropical Atlantic (see Fig. 8 for integral areas).

To assess how the spatial origins of  $AMOC_{25N}$  variability differ across the reanalysis ensemble, we plot the ensemble range of time-integrated absolute  $AMOC_{25N}$  anomalies for each force in Figs. 8e–h. In general, regions where large  $AMOC_{25N}$  variability is generated by each air–sea flux are also regions where air–sea flux uncertainty projects onto large uncertainty (ensemble spread) in  $AMOC_{25N}$ , though the latter is dominated by forcing uncertainty close to the basin boundaries. Notably, zonal-wind uncertainty over the subpolar gyre is responsible for one-quarter of the total uncertainty in the time-integrated zonal-wind-driven  $AMOC_{25N}$ . Uncertainties in heat and freshwater fluxes over the subpolar gyre are also very important, contributing approximately one-half and one-third, respectively, to the ensemble spread in the associated time-integrated absolute  $AMOC_{25N}$  anomaly. These fractional contributions of subpolar air–sea flux uncertainty to total  $AMOC_{25N}$  uncertainty are the same as the fractional contributions of subpolar air–sea fluxes to the total  $AMOC_{25N}$  variability. Note that at most grid cells, the  $AMOC_{25N}$  spread (Figs. 8e–h) generated by local air–sea flux uncertainty is of a similar amplitude to the reanalysis ensemble mean estimate of  $AMOC_{25N}$  variability (Figs. 8a–d).

To further illustrate that the generation of  $AMOC_{25N}$  uncertainty is largely mediated by ocean dynamics (i.e., the linear sensitivity patterns) and not entirely governed by where the air–sea flux uncertainty is largest, we map the ensemble range of the time-integrated absolute forcing anomaly as used in the  $AMOC_{25N}$  variability calculation [Eq. (2)] in Figs. 8i–l.<sup>2</sup> The largest uncertainties in reanalysis Atlantic wind stress are found

adjacent to the western boundary at all latitudes (Figs. 8i,l),<sup>3</sup> but only impact the  $AMOC_{25N}$  estimate north of 25°N (Figs. 8e,f). Although the subpolar gyre was shown to be an important source region for externally forced  $AMOC_{25N}$  uncertainty, only 7% of the total reanalysis uncertainty in Atlantic zonal wind stress is found here (Fig. 8i).

Reanalysis uncertainty in the Atlantic surface freshwater flux is largest throughout the deep tropics and along the western boundary in the South Atlantic (Fig. 8l). Uncertainty in the tropics alone accounts for approximately two-thirds of the total Atlantic surface freshwater flux uncertainty (see Fig. 8l for integral area). Only the tropical freshwater flux uncertainty in the western equatorial waveguides has a notable impact on  $AMOC_{25N}$ , generating approximately one-third of the total freshwater-flux-driven  $AMOC_{25N}$  ensemble spread (Fig. 8h). Reanalysis uncertainty in freshwater fluxes over the North Atlantic is much smaller than over the deep tropics (Fig. 8l); freshwater flux uncertainty over the subpolar gyre accounts for only one-tenth of the total Atlantic surface freshwater flux uncertainty but, as noted above, has a disproportionately large impact on the total freshwater-flux-driven  $AMOC_{25N}$  spread (Fig. 8h).

Reanalysis uncertainty in Atlantic surface heat flux is largest along the Gulf Stream and separation region and in the subpolar basin (Fig. 8k). On decadal time scales it has been shown that  $AMOC_{25N}$  is sensitive to surface buoyancy forcing throughout these regions (Czeschel et al. 2010; Heimbach et al. 2011; Pillar et al. 2016), associated with the excitation of a thermal Rossby mode (Huck et al. 1999; Te Raa and Dijkstra 2002). Forcing uncertainty along this pathway generates large ensemble spread in  $AMOC_{25N}$  (Fig. 8g). Heat flux uncertainty over the subpolar gyre accounts for one-quarter of the total Atlantic surface heat flux uncertainty in the reanalysis ensemble (Fig. 8k) but, as noted above, approximately one-half of the total heat-flux-driven  $AMOC_{25N}$  spread is generated here (Fig. 8g).

## 5. Refining key uncertainty targets

We now seek to consolidate our separate analyses of the space and time origins of ensemble spread in  $AMOC_{25N}$  presented above and identify critical reductions in air–sea flux uncertainty for improved modeling of  $AMOC_{25N}$ . We start by refining our assessment of the key areas of wind-forcing uncertainty presented in

<sup>2</sup> This metric is chosen to facilitate comparison with the spatial origins of  $AMOC_{25N}$  uncertainty shown in Figs. 8e–h. Note that since the  $AMOC_{25N}$  calculation for the period January 1994–December 2011 accounts for the  $AMOC_{25N}$  response to forcing at lead times of up to 15 yr [Eq. (2)], the spatial origins of forcing uncertainty are assessed for the period January 1979–December 2011.

<sup>3</sup> Boundary uncertainty is likely due in part to the interpolation of ensemble members from different native grids.



section 4d, to map only the spread generated at the key times identified in sections 4b and 4c. In Fig. 5 we saw that uncertainties in zonal wind forcing dominate the  $AMOC_{25N}$  spread at lags of 0–6.5 yr. This wind-driven  $AMOC_{25N}$  spread was shown to be largely a response to concurrent zonal-wind stress uncertainty ( $AMOC_{25N}$  lag = 1 month; Fig. 4a). Furthermore, September zonal-wind uncertainties appear to be most potent (Fig. 7a), although the factors controlling this seasonality were not explored. Following these results, we examine the time-mean spatial origins and seasonality of ensemble spread in  $AMOC_{25N}$  generated by uncertainty in the concurrent zonal winds ( $AMOC_{25N}$  lag = 1 month) in Figs. 9a–f. The time-mean seasonality in zonal-wind forcing uncertainty is shown in Figs. 9m–r. The time averages are computed for the period common to the reanalysis ensemble (January 1979–December 2011). We show the linear sensitivity of  $AMOC_{25N}$  to concurrent zonal wind forcing [ $\partial\bar{\psi}^{\text{month}}/\partial\tau^x(x, y, T_{\text{lead}} = 1 \text{ month})$ ] in Figs. 9g–l.

Clearly, the generation of  $AMOC_{25N}$  uncertainty by the zonal-wind uncertainty is largely shaped by the linear sensitivity patterns, but the seasonality is in part set by the forcing uncertainty. Most importantly, the largest zonal-wind-driven spread in  $AMOC_{25N}$  occurs during September and is driven mainly (i) in the eastern boundary waveguides between the equator and 12°N and (ii) throughout the western half of the basin at 25°N (Fig. 9e). Although September sensitivities are much larger than the annual average over (i) the eastern boundary waveguides, they are smaller than average over (ii) the western half of the Atlantic basin at 25°N (Fig. 9k). However, in both of these regions, the zonal-wind uncertainty is largest during September (Fig. 9q), explaining the September occurrence of the maximum zonal-wind-driven  $AMOC_{25N}$  uncertainty.

In Figs. 11a and 11b we identify the reanalysis products providing the upper and lower bounds on the September zonal wind stress estimates. Dynamically potent zonal-wind stress uncertainty along 25°N, and through the upstream coastal waveguides, is due largely to an offset of the 20CR product from the NCEP-based and ERA-INT estimates. Averaged over all September months from 1979 to 2011, 20CR provides the lower bound on the reanalyzed eastward zonal wind stress in these regions, while the upper bound is provided by a combination of NCEPI, NCEPII, and ERA-INT.

We now try to refine our assessment of the critical areas in which to reduce the air–sea buoyancy flux uncertainty. This is more challenging due to the diffuse time origins of buoyancy-driven  $AMOC_{25N}$  ensemble spread, which we have shown accumulates gradually with lag from the causal forcing uncertainty (Figs. 4c,d), although February buoyancy flux uncertainties appear

most potent at all lags (Figs. 7c,d). To proceed, we focus on heat flux uncertainties, which dominate the total  $AMOC_{25N}$  ensemble spread at lags exceeding 6.5 yr (Fig. 5, solid red line). Furthermore, we focus on the  $AMOC_{25N}$  response at a lag of around 7 yr, when heat flux uncertainties are most potent (Fig. 5, dashed red line).

In Figs. 10a–f we plot the time-mean spatial origins and seasonality of the  $AMOC_{25N}$  ensemble spread generated by surface heat fluxes at  $AMOC_{25N}$  lag = 7–8 yr. The time-mean seasonality in surface heat flux uncertainty is shown in Figs. 10m–r. The time averages are computed for the period common to the reanalysis ensemble (January 1987–December 2011). In Figs. 10g–l we show the linear sensitivity of  $AMOC_{25N}$  to surface heat forcing at a lead time of 7–8 yr. Seasonality in  $AMOC_{25N}$  spread and  $AMOC_{25N}$  linear sensitivity can be assessed by the month in which  $AMOC_{25N}$  occurs, or the month in which the causal forcing occurs. Since the  $AMOC_{25N}$  uncertainty calculation in a given year varies more strongly with small shifts in the seasonal timing of the forcing than with small shifts in the seasonal timing of the  $AMOC_{25N}$ , we assess seasonality with regard to the month in which the causal forcing occurs in Fig. 10. The  $AMOC_{25N}$  spread (Figs. 10a–f) and linear sensitivity (Figs. 10g–l) are shown only for the January  $AMOC_{25N}$ , but the qualitative information provided by Fig. 10 does not depend on the month in which the  $AMOC_{25N}$  is defined.

The key result from Fig. 10 is that the largest surface heat-flux-driven  $AMOC_{25N}$  spread is forced in February, over the subpolar gyre, with isolated maxima in uncertainty generation in the Labrador Sea and to the south and east of Iceland (Fig. 10a). These hotspots of uncertainty generation are collocated with locally large sensitivities (Fig. 10g) over convectively active regions in the model (not shown) and consistent with published results highlighting the importance of initializing Labrador Sea Water anomalies for skillful forecasting of AMOC on decadal time scales (Yeager et al. 2012; Msadek et al. 2014; Yeager et al. 2015). The timing is due both to seasonally larger-amplitude sensitivities in these regions (Fig. 10g) and the occurrence of the maximum uncertainty in high-latitude surface heat fluxes in February (Fig. 10m). This timing also appears physically reasonable as it slightly precedes the onset of Labrador Sea convection in both observations (Lilly et al. 1999) and our model. It is also consistent with recent work by Jones et al. (2018), showing that Labrador Sea heat content is most sensitive to surface heat fluxes occurring 1 month before the mixed layer depth maximum. As explained by Jones et al. (2018), heat flux anomalies slightly preceding convective adjustment have the

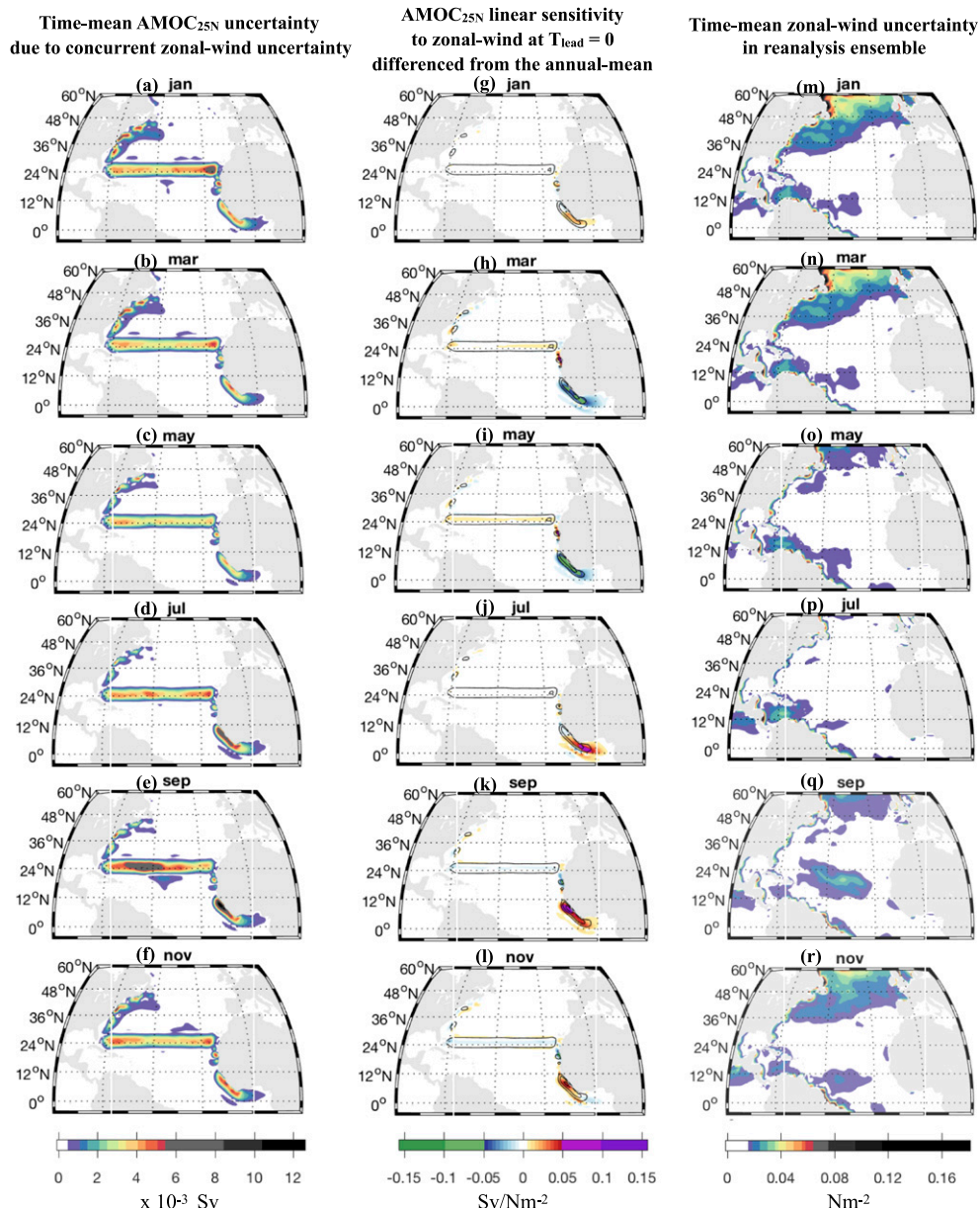


FIG. 9. Comparison of seasonality in (left)  $AMOC_{25N}$  uncertainty ( $Sv$ ) generated by concurrent zonal-wind uncertainty, (middle)  $AMOC_{25N}$  linear sensitivity to concurrent zonal winds [ $Sv (Nm^{-2})^{-1}$ ], and (right) reanalysis zonal-wind uncertainty ( $Nm^{-2}$ ). The aim is to determine whether seasonality in (left) wind-driven  $AMOC_{25N}$  uncertainty generation is set by (right) when the wind forcing is most uncertain or (middle) when the ocean is most sensitive to wind forcing anomalies. In each column we show 6 of the 12 months of the year and focus on the North Atlantic, where wind-driven  $AMOC_{25N}$  uncertainty is largest (Fig. 8e). In the left and right columns the time-mean seasonality is shown, computed for the period common to the reanalysis ensemble. For example, in (a) we compute the ensemble range of the January  $AMOC_{25N}$  driven by concurrent (January) zonal winds, for all January months between 1979 and 2011, then plot the average range; in (m) we compute the ensemble range of reanalysis zonal winds in January, for all Januaries between 1979 and 2011, then plot the average range. The seasonal cycle in sensitivity is relatively small compared to the annual mean sensitivity, but is nevertheless important in setting the seasonality of the  $AMOC_{25N}$  uncertainty. For this reason, we plot the monthly sensitivity anomaly in the middle column, to highlight the seasonal maxima (positive values, shaded red to purple). The monthly sensitivity anomaly (shaded) is defined as the absolute monthly sensitivity [contoured with an interval of  $0.2 Sv (Nm^{-2})^{-1}$ ] differenced from the absolute annual-mean sensitivity. In (g)–(l) note that the sign indicates whether the absolute amplitude of the monthly sensitivity is larger (positive values) or smaller (negative values) than the absolute annual mean. It is important to stress that it does not indicate whether  $AMOC_{25N}$  will strengthen or weaken in response to a local change in zonal-wind stress.

largest impact on local ocean heat content as they are mixed over the largest vertical extent of the water column.

In Figs. 11c and 11d we identify the reanalysis products providing the maximum and minimum February surface heat flux estimates, averaged over the years 1979–2011. Dynamically potent heat flux uncertainty in the Labrador Sea is largely due to differences between ERA-INT and NCEP2. On average, ERA-INT and NCEP2 provide the upper and lower bounds, respectively, on the reanalyzed estimates of upward heat flux over the Labrador Sea.

It is important to note here that the modeled response to high-latitude surface buoyancy changes may be particularly susceptible to corruption by the restoring of sea surface temperature and salinity (Y. Kostov 2018, personal communication). Due to the strong sensitivity of seawater density to small perturbations in salinity at low temperatures, evaporative feedbacks can quickly compensate for heat-flux-induced surface density changes at high latitude. Ongoing work highlights that this compensation is strongly seasonal (due to mixed layer depth seasonality) and acutely sensitive to surface restoring (Y. Kostov et al. 2018, unpublished manuscript). This delicate interplay between surface heat and freshwater fluxes, mixed layer depth, and surface restoring is highly nonlinear and unlikely to be well represented in our experiment configuration (Y. Kostov 2018, personal communication), remaining an important topic for further research.

Finally, we note that what we describe as “wind driven”  $AMOC_{25N}$  uncertainty accounts only for the impact of uncertain air–sea momentum fluxes. In reality, wind uncertainty contributes to the “buoyancy driven”  $AMOC_{25N}$  uncertainty, through the dependence of evaporation and surface heat fluxes on wind speed. We are not able to assess this contribution with our current experiment design. Valuable insights into this issue will be offered in an upcoming study (Smith and Heimbach 2018, manuscript submitted to *J. Climate*), in which recent variability in the AMOC at 34°S is attributed to past changes in atmospheric forcing. This adjoint-based attribution study uses an observationally constrained model forced by bulk formulas. The authors are therefore able to quantify the sensitivity of the AMOC at 34°S to uncertainty in the individual atmospheric state variables (wind speed, humidity, etc.) used in the bulk formulas.

## 6. Discussion and conclusions

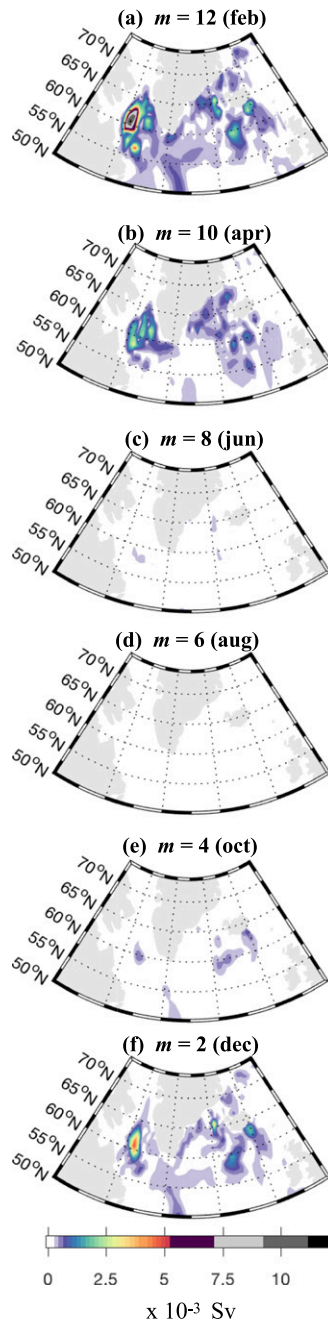
Atmospheric reanalyses are commonly used to provide air–sea fluxes of buoyancy and momentum to drive

OGCMs. Although independent reanalyses assimilate many of the same observational datasets, notable discrepancies exist between products. These have been well documented in the scientific literature. The impact of these discrepancies on the simulated ocean state has received less attention to date. In this study, we have explored the impact of reanalysis air–sea flux uncertainty—applied over a 15-yr period—on the simulated ocean state. We have focused on variability in Atlantic meridional overturning circulation about the mean seasonal cycle at 25°N ( $AMOC_{25N}$ ). This is a natural extension of our earlier study (Pillar et al. 2016), in which we present model-based linear sensitivities of  $AMOC_{25N}$  to air–sea fluxes at lead times of up to 15 yr and discuss the adjustment mechanisms revealed in the temporal and spatial evolution of the sensitivity patterns.

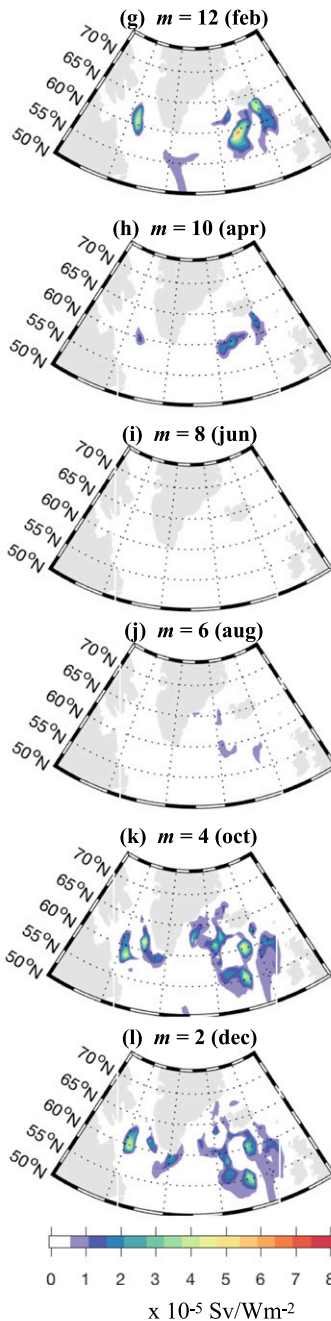
Here, we have projected forcing anomalies from five atmospheric reanalysis products onto the linear sensitivity patterns to construct five time series of  $AMOC_{25N}$  anomalies. Throughout most of the paper, we have focused on the period January 1994–December 2011, where an  $AMOC_{25N}$  estimate constructed using a 15-yr forcing history was available at the time of our investigation for all five reanalyses. By differencing  $AMOC_{25N}$  variability estimates across the ensemble, we are able to make separate quantitative assessments of the uncertainty in  $AMOC_{25N}$  that originates from uncertainty in reanalysis zonal wind stress, meridional wind stress, surface heat fluxes, and surface freshwater fluxes. Furthermore, our approach has allowed us to explore where and when atmospheric forcing uncertainty generates the largest uncertainty (ensemble spread) in  $AMOC_{25N}$ .

Our ensemble of  $AMOC_{25N}$  estimates shows good qualitative agreement, notably in the timing of high-amplitude zonal-wind-driven  $AMOC_{25N}$  anomalies and apparent low-frequency trends driven by surface buoyancy forcing (Fig. 1). However, the ensemble spread in  $AMOC_{25N}$  induced by prior air–sea flux uncertainty can exceed 4 Sv within 15 yr, at times exceeding the amplitude of the ensemble-mean  $AMOC_{25N}$  anomaly (Fig. 2). On average, this spread increases monotonically with time; after a 15-yr period, the  $AMOC_{25N}$  spread induced by uncertainty in the zonal wind, meridional wind, surface heat flux, and surface freshwater flux is 0.8, 0.5, 2.2, and 0.8 Sv, respectively (Fig. 4). However, there is a notable difference in the evolution of the wind and buoyancy-induced ensemble spread. Whereas the former is dominated by a rapid  $AMOC_{25N}$  adjustment to local wind uncertainties at short lead, and becomes less important with increasing  $AMOC_{25N}$  lag, the latter is dominated by slow  $AMOC_{25N}$

**Time-mean January AMOC<sub>25N</sub> uncertainty due to surface heat flux uncertainty at  $T_{\text{lead}} = 7 \text{ years} + m \text{ months}$**



**January AMOC<sub>25N</sub> linear sensitivity to surface heat flux at  $T_{\text{lead}} = 7 \text{ years} + m \text{ months}$**



**Time-mean surface heat flux uncertainty in reanalysis ensemble**

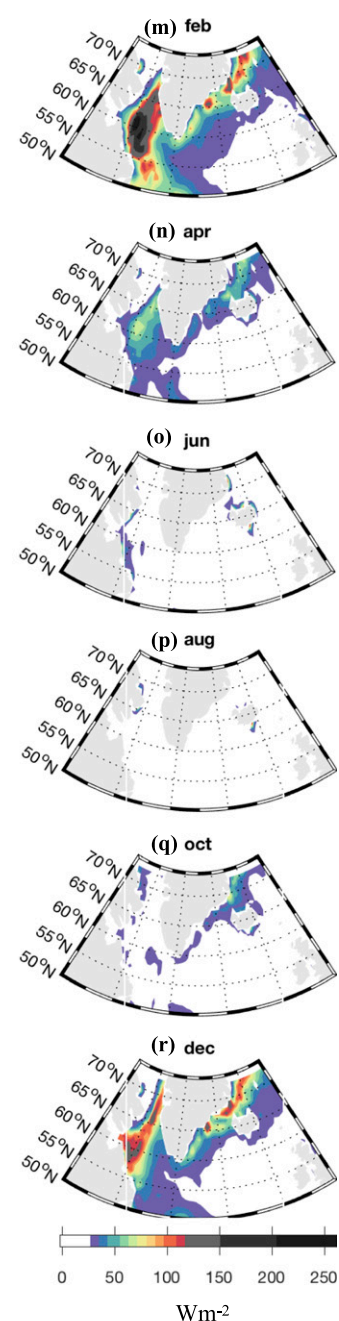


FIG. 10. Comparison of seasonality in (left) January AMOC<sub>25N</sub> uncertainty (Sv) generated by surface heat flux uncertainty at a lead time of 7 yr +  $m$  months, (middle) AMOC<sub>25N</sub> absolute linear sensitivity to surface heat fluxes at a lead time of 7 yr +  $m$  months  $\text{Sv} (\text{W m}^{-2})^{-1}$ , and (right) reanalysis surface heat flux uncertainty in the indicated month ( $\text{W m}^{-2}$ ). In the left and middle columns the corresponding month of the causal forcing is given in brackets. The aim is to determine whether seasonality in heat-flux-driven AMOC<sub>25N</sub> uncertainty (left column) is set by when the heat forcing is most uncertain (right column) or when the ocean is most sensitive to heat flux anomalies (middle column). In each column we show 6 of the 12 months of the year and focus on the high-latitude North Atlantic, where heat-flux-driven AMOC<sub>25N</sub> uncertainty is largest. In the left and right columns the time-mean seasonality is shown, computed for the period common to the reanalysis ensemble. For example, in (a) we compute the ensemble range of the January AMOC<sub>25N</sub> driven by February surface heat fluxes at a lead time of 8 yr, for all January months between 1985 and 2011, then plot the average range. In (g) we plot the sensitivity of the January AMOC<sub>25N</sub> to the February surface heat flux 8 yr earlier  $[\partial\bar{\psi}^{\text{Jan}}/\partial Q(x, y, T_{\text{lead}}) = 8 \text{ yr}]$ . In (m) we compute the ensemble range of reanalysis surface heat flux in February, for all February months between 1979 and 2011, then plot the average range.

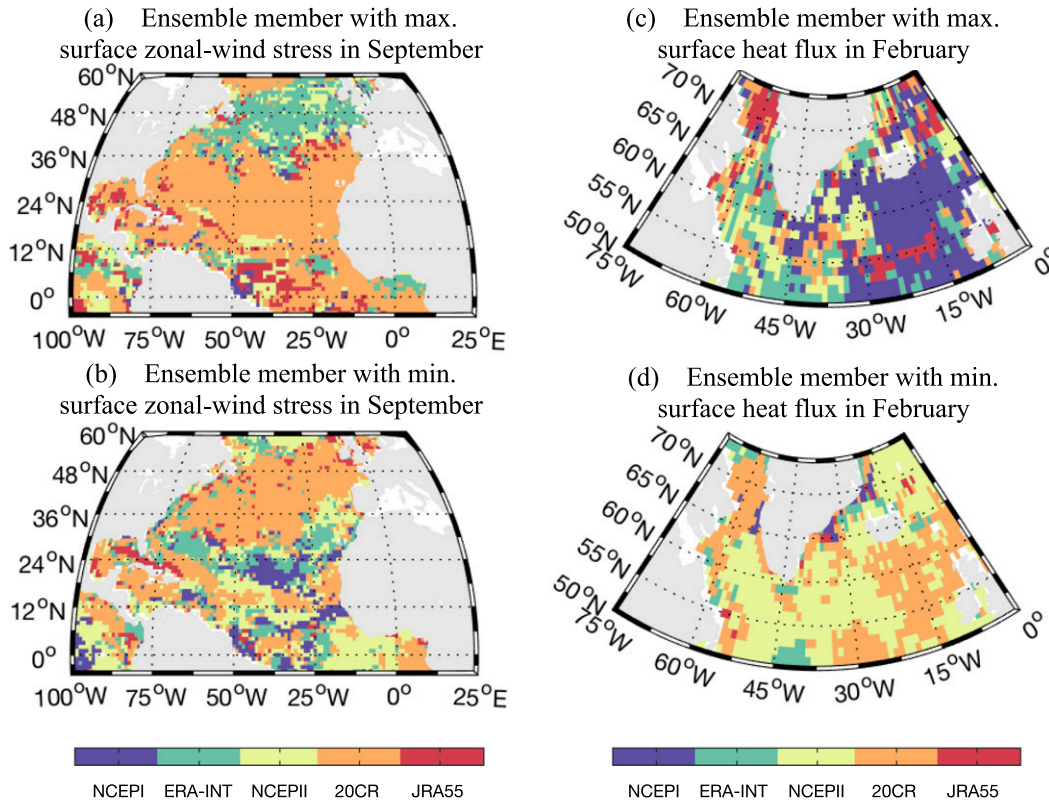


FIG. 11. Reanalysis product providing the (a),(c) maximum and (b),(d) minimum estimated (a),(b) September zonal wind stress and (c),(d) February surface heat flux, on average, during the period 1979–2011. We show only those regions where significant  $AMOC_{25N}$  uncertainty is generated by uncertainty in the zonal wind [(a),(b)] and surface heat flux [(c),(d)], for direct comparison with Figs. 9e and 10a, respectively. For example, heat-flux-driven uncertainty in  $AMOC_{25N}$  is largely influenced by heat-flux uncertainty over the Labrador Sea in February (Figs. 7c and 10a). Uncertainty in the surface heat fluxes is substantial here (Fig. 10m), due mainly to differences between ERA-INT and NCEPII [(c),(d)]. On average, ERA-INT and NCEPII provide the upper and lower bounds, respectively, on the reanalysis estimates of upward heat flux over the Labrador Sea in February. Note that for a small selection of grid cells, the same product provides both the time-mean (modal) upper and lower bounds on the forcing estimate [e.g., NCEPII, Labrador Sea in (c),(d)].

adjustment to surface heat flux uncertainty over the subpolar latitudes and becomes increasingly important with  $AMOC_{25N}$  lag (Fig. 4). A key result is that, on average,  $AMOC_{25N}$  uncertainty is dominated by uncertainty in the zonal wind at lags of up to 6.5 yr, and by uncertainty in surface heat fluxes thereafter (Fig. 5). Furthermore, although Atlantic zonal-wind stress uncertainties are largest along the western boundary and throughout the North Atlantic subpolar gyre (Fig. 8i), they are most potent in the vicinity of 25°N (Fig. 9). Atlantic surface heat flux uncertainties are largest along the Gulf Stream and throughout the subpolar ocean (Fig. 8k), but are most potent in the Labrador Sea (Fig. 10).

Our study is limited in that we are only able to consider a 15-yr-long  $AMOC_{25N}$  response history using the adjoint. On longer time scales, air–sea flux uncertainties would

continue to impact our  $AMOC_{25N}$  estimate (Figs. 4a–d) through slower advective teleconnections (e.g., Thomas et al. 2015) and it is possible that remote uncertainties, for example, in air–sea fluxes over the Antarctic Circumpolar Current, could become more important (e.g., Nikurashin and Vallis 2012). Furthermore, we neglect the impact of systematic offsets between the reanalysis products in our estimation of externally forced  $AMOC_{25N}$  uncertainty. This omission occurs because the forcing anomaly for any product,  $i$ , is computed about the climatological seasonal cycle in that same product [Eq. (1)]. Since product differences in seasonal climatology (e.g.,  $F_{ERA-INT}^{sc} - F_{NCEPII}^{sc}$ ) are substantial, a rigorous investigation of the resulting uncertainty in  $AMOC_{25N}$  is an important avenue for future research.

An additional caveat of our study is the use of smoothed forcing: both 1) the climatological forcing

used in the spinup integration and 2) the forcing anomalies projected onto the linear sensitivities are monthly values. High-frequency atmospheric variability, not included in our model, is thought to play a critical role in ocean convective variability (e.g., [Pickart et al. 2008](#); [Våge et al. 2009](#)). Here, we have identified Labrador Sea heat flux uncertainty as an important driver of AMOC<sub>25N</sub> uncertainty, but should validate this result in future work, using a model with a better representation of synoptic air–sea flux variations (e.g., [Jones et al. 2018](#); [Smith and Heimbach 2018](#), manuscript submitted to *J. Climate*).

Our results are also subject to any deficiencies in the OGCM, leading to a misrepresentation of the AMOC<sub>25N</sub> adjustment to air–sea fluxes. Importantly, the strongest response of AMOC<sub>25N</sub> to uncertainties over the North Atlantic subpolar gyre is set by the principal convecting regions and dominant time scale of internal variability in the model ([Delworth and Zeng 2016](#)). These vary significantly from model to model ([Zhang and Wang 2013](#); [MacMartin et al. 2013](#); [Branstator and Teng 2012](#)), due to biases in the mean state (e.g., [Drews and Greatbatch 2016](#)), insufficient model resolution ([Marshall and Johnson 2013](#); [Thomas and Zhai 2013](#); [Shaffrey et al. 2017](#)), uncertain model parameterizations ([Farneti and Vallis 2011](#); [Yeager and Danabasoglu 2012](#); [Danabasoglu et al. 2012](#)), and the restoration of temperature and salinity ([Latif et al. 2006](#); [Behrens et al. 2013](#); [Zhai et al. 2014](#)). Lacking sufficiently long observational time series and consensus on the responsible mechanisms ([Buckley and Marshall 2016](#)), it remains a challenge to assess model reliability in simulating low-frequency AMOC variability, highlighting the importance of sustaining continuous observations of North Atlantic overturning and deep water formation [e.g., at the RAPID and Overturning in the Subpolar North Atlantic Program (OSNAP) arrays; see [McCarthy et al. \(2015\)](#) and [Lozier et al. \(2017\)](#), respectively]. Restoration of sea surface temperature and salinity may also impact the seasonality of the sensitivity (Y. Kostov 2018, personal communication) and alter the seasonal potency of the reanalysis uncertainty discussed in [section 4c](#). Finally, we note that due to the strong sensitivity of AMOC<sub>25N</sub> to density variations at the east and west boundaries, our results may be sensitive to the chosen method of interpolating the atmospheric reanalyses onto the ocean model grid.

Despite these limitations, the time scales and regions of externally forced AMOC<sub>25N</sub> uncertainty appear plausible in bearing many similarities to time scales and regions of externally forced AMOC variability in the scientific literature. In particular, the dominance of subpolar heat fluxes in driving decadal North Atlantic overturning variability is in agreement with published

studies exploring the AMOC response to the North Atlantic Oscillation, using idealized ([Zhai et al. 2014](#)), geographically realistic ([Böning 2006](#); [Biastoch et al. 2008](#); [Yeager and Danabasoglu 2014](#)), and fully coupled ([Delworth et al. 2016](#)) nonlinear models. The critical importance of local heat flux forcing over the deep convection regions is consistent with AMOC estimates presented by [Yeager and Danabasoglu \(2014\)](#), who show that variations in air–sea buoyancy exchange over the Labrador Sea interior alone drive almost all decadal variability in the modeled AMOC from 1958 to 2007.

We find that uncertainty in reanalyzed surface momentum and buoyancy fluxes can produce net uncertainties as large as  $\sim 5$  Sv in the modeled AMOC<sub>25N</sub>. For the time period considered, the time-averaged externally forced AMOC<sub>25N</sub> uncertainty is  $\sim 2$  Sv. Recalling once again that our buoyancy-driven AMOC<sub>25N</sub> estimates do not converge as we increase the time window over which we perform the convolution, we stress that the amplitude of AMOC<sub>25N</sub> uncertainty reported here may continue to change, and may even decrease, when accounting for the AMOC<sub>25N</sub> response over a longer time window.

Interestingly, however, our estimates are consistent with the existing estimates of atmosphere-forced AMOC uncertainty ([Brodeau et al. 2010](#); [He et al. 2016](#)), discussed in [section 2](#). Most importantly, the amplitude of the externally forced AMOC<sub>25N</sub> uncertainty presented here is comparable to the AMOC uncertainty in the COREv2-forced hindcasts ([Danabasoglu et al. 2016](#)), where the ensemble of AMOC estimates exhibits a time-mean standard deviation of  $\sim 3$  Sv about the ensemble mean. Since these hindcasts share a common atmospheric forcing history, AMOC divergence across the ensemble is due to model differences alone. Recently, [Huber and Zanna \(2017\)](#) have demonstrated air–sea flux uncertainty is at least as important as parameter uncertainty in driving divergence in the steady-state AMOC in the Coupled Model Intercomparison Project phase 5. Our results give further support to their claim that atmospheric forcing uncertainty is a key source of ocean uncertainty in climate models and hence a key area to target now for improved skill in future climate prediction.

*Acknowledgments.* The authors would like to acknowledge the use of the Advanced Research Computing (ARC) facility in carrying out this work. The MITgcm and its adjoint are available online (<http://mitgcm.org/>). The NCEPI, NCEPII, and 20CR reanalysis products are available for download at <https://www.esrl.noaa.gov/psd/data/gridded/reanalysis/>. The ERA-INT reanalysis can be downloaded at <https://www.ecmwf.int/en/forecasts/datasets/archive-datasets/>

reanalysis-datasets/era-interim. The JRA55 reanalysis can be downloaded at <https://rda.ucar.edu/datasets/ds628.1/>. We thank three anonymous reviewers for comments that greatly improved the manuscript. We are grateful to Yavor Kostov and Matthew Thomas for helpful discussion. We thank David Munday, Laure Zanna, Mirosław Andrejczuk, and Lars Czeschel for generously sharing advice on running the MITgcm and its adjoint. We are grateful to Riccardo Farneti for providing output from the COREv2-forced ensemble for closer inspection. HLJ and DPM acknowledge the partial support of the U.K. Natural Environment Research Council (NE/K010948/1). PH received partial support from the NSF (Grant 1603903), NOAA (Grant NA130AR4310135), and NASA via a JPL/Caltech subcontract [Estimating the Circulation and Climate of the Ocean (ECCO)]. ST was funded by a Met Office Academic Partnership summer research experience placement.

## REFERENCES

- Antonov, J. I., and Coauthors, 2010: *Salinity*. Vol. 2, *World Ocean Atlas 2009*, NOAA Atlas NESDIS 69, 184 pp., [ftp://ftp.nodc.noaa.gov/pub/WOA09/DOC/woa09\\_vol2\\_text.pdf](ftp://ftp.nodc.noaa.gov/pub/WOA09/DOC/woa09_vol2_text.pdf).
- Årthun, M., T. Eldevik, E. Viste, H. Drange, T. Furevik, H. L. Johnson, and N. S. Keenlyside, 2017: Skillful prediction of northern climate provided by the ocean. *Nat. Commun.*, **8**, 15875, <https://doi.org/10.1038/ncomms15875>.
- Behrens, E., A. Biastoch, and C. Böning, 2013: Spurious AMOC trends in global ocean sea-ice models related to subarctic freshwater forcing. *Ocean Modell.*, **69**, 39–49, <https://doi.org/10.1016/j.ocemod.2013.05.004>.
- Bengtsson, L., S. Hagemann, and K. Hodges, 2004a: Can climate trends be calculated from reanalysis data? *J. Geophys. Res.*, **109**, D11111, <https://doi.org/10.1029/2004JD004536>.
- , K. Hodges, and S. Hagemann, 2004b: Sensitivity of the ERA40 reanalysis to the observing system: Determination of the global atmospheric circulation from reduced observations. *Tellus*, **56A**, 456–471, <https://doi.org/10.3402/tellusa.v56i5.14466>.
- , and Coauthors, 2007: The need for a dynamical climate reanalysis. *Bull. Amer. Meteor. Soc.*, **88**, 495–501, <https://doi.org/10.1175/BAMS-88-4-495>.
- Bentsen, M., H. Drange, T. Furevik, and T. Zhou, 2004: Simulated variability of the Atlantic meridional overturning circulation. *Climate Dyn.*, **22**, 701–720, <https://doi.org/10.1007/s00382-004-0397-x>.
- Biastoch, A., C. W. Böning, J. Getzlaff, J.-M. Molines, and G. Madec, 2008: Causes of interannual–decadal variability in the meridional overturning circulation of the North Atlantic Ocean. *J. Climate*, **21**, 6599–6615, <https://doi.org/10.1175/2008JCLI2404.1>.
- Blaker, A. T., J.-M. Hirschi, G. McCarthy, B. Sinha, S. Taws, B. Marsh, A. Coward, and B. de Cuevas, 2015: Historical analogues of the recent extreme minima observed in the Atlantic meridional overturning at 26°N. *Climate Dyn.*, **44**, 457–473, <https://doi.org/10.1007/s00382-014-2274-6>.
- Böning, C., 2006: Decadal variability of subpolar gyre transport and its reverberation in the North Atlantic overturning. *Geophys. Res. Lett.*, **33**, L21S01, <https://doi.org/10.1029/2006GL026906>.
- Branstator, G., and H. Teng, 2012: Potential impact of initialization on decadal predictions as assessed for CMIP5 models. *Geophys. Res. Lett.*, **39**, L12703, <https://doi.org/10.1029/2012GL051974>.
- Brodeau, L., B. Barnier, A. Treguier, T. Penduff, and S. Gulev, 2010: An ERA40-based atmospheric forcing for global ocean circulation models. *Ocean Modell.*, **31**, 88–104, <https://doi.org/10.1016/j.ocemod.2009.10.005>.
- Brunke, M., Z. Wang, X. Zeng, M. Bosilovich, and C.-L. Shie, 2011: An assessment of the uncertainties in ocean surface turbulent fluxes in 11 reanalysis, satellite-derived, and combined global datasets. *J. Climate*, **24**, 5469–5493, <https://doi.org/10.1175/2011JCLI4223.1>.
- Buckley, M., and J. Marshall, 2016: Observations, inferences, and mechanisms of Atlantic Meridional Overturning Circulation variability: A review. *Rev. Geophys.*, **54**, 5–63, <https://doi.org/10.1002/2015RG000493>.
- Chaudhuri, A., R. Ponte, G. Forget, and P. Heimbach, 2013: A comparison of atmospheric reanalysis surface products over the ocean and implications for uncertainties in air–sea boundary forcing. *J. Climate*, **26**, 153–170, <https://doi.org/10.1175/JCLI-D-12-00090.1>.
- , —, and —, 2016: Impact of uncertainties in atmospheric boundary conditions on ocean model solutions. *Ocean Modell.*, **100**, 96–108, <https://doi.org/10.1016/j.ocemod.2016.02.003>.
- Compo, G., and Coauthors, 2011: The Twentieth Century Reanalysis Project. *Quart. J. Roy. Meteor. Soc.*, **137**, 1–28, <https://doi.org/10.1002/qj.776>.
- Cunningham, S., and Coauthors, 2007: Temporal variability of the Atlantic meridional overturning circulation at 26.5°N. *Science*, **317**, 935–938, <https://doi.org/10.1126/science.1141304>.
- Czeschel, L., D. P. Marshall, and H. L. Johnson, 2010: Oscillatory sensitivity of the Atlantic overturning to high-latitude forcing. *Geophys. Res. Lett.*, **37**, L10601, <https://doi.org/10.1029/2010GL043177>.
- , C. Eden, and R. J. Greatbatch, 2012: On the driving mechanism of the annual cycle of the Florida Current transport. *J. Phys. Oceanogr.*, **42**, 824–839, <https://doi.org/10.1175/JPO-D-11-0109.1>.
- Dai, A., and K. Trenberth, 2002: Estimates of freshwater discharge from continents: Latitudinal and seasonal variations. *J. Hydrometeorol.*, **3**, 660–687, [https://doi.org/10.1175/1525-7541\(2002\)003<0660:EOFDFC>2.0.CO;2](https://doi.org/10.1175/1525-7541(2002)003<0660:EOFDFC>2.0.CO;2).
- Danabasoglu, G., S. Yeager, Y.-O. Kwon, J. Tribbia, A. Phillips, and J. Hurrell, 2012: Variability of the Atlantic meridional overturning circulation in CCSM4. *J. Climate*, **25**, 5153–5172, <https://doi.org/10.1175/JCLI-D-11-00463.1>.
- , and Coauthors, 2016: North Atlantic simulations in Coordinated Ocean-ice Reference Experiments phase II (CORE-II). Part II: Inter-annual to decadal variability. *Ocean Modell.*, **97**, 65–90, <https://doi.org/10.1016/j.ocemod.2015.11.007>.
- Dee, D., 2005: Bias and data assimilation. *Quart. J. Roy. Meteor. Soc.*, **131**, 3323–3343, <https://doi.org/10.1256/qj.05.137>.
- , and Coauthors, 2011: The ERA-Interim reanalysis: Configuration and performance of the data assimilation system. *Quart. J. Roy. Meteor. Soc.*, **137**, 553–597, <https://doi.org/10.1002/qj.828>.
- Delworth, T., and M. Mann, 2000: Observed and simulated multidecadal variability in the Northern Hemisphere. *Climate Dyn.*, **16**, 661–676, <https://doi.org/10.1007/s003820000075>.
- , and F. Zeng, 2016: The impact of the North Atlantic Oscillation on climate through its influence on the Atlantic

- meridional overturning circulation. *J. Climate*, **29**, 941–962, <https://doi.org/10.1175/JCLI-D-15-0396.1>.
- , —, G. Vecchi, X. Yang, L. Zhang, and R. Zhang, 2016: The North Atlantic Oscillation as a driver of rapid climate change in the Northern Hemisphere. *Nat. Geosci.*, **9**, 509–512, <https://doi.org/10.1038/ngeo2738>.
- Dessler, A., and S. Davis, 2010: Trends in tropospheric humidity from reanalysis systems. *J. Geophys. Res.*, **115**, D19127, <https://doi.org/10.1029/2010JD014192>.
- Draws, A., and R. Greatbatch, 2016: Atlantic multidecadal variability in a model with an improved North Atlantic current. *Geophys. Res. Lett.*, **43**, 8199–8206, <https://doi.org/10.1002/2016GL069815>.
- Ebita, A., and Coauthors, 2011: The Japanese 55-year Reanalysis “JRA-55”: An interim report. *SOLA*, **7**, 149–152, <https://doi.org/10.2151/sola.2011-038>.
- Eden, C., and J. Willebrand, 2001: Mechanisms of interannual to decadal variability of the North Atlantic circulation. *J. Climate*, **14**, 2266–2280, [https://doi.org/10.1175/1520-0442\(2001\)014<2266:MOITDV>2.0.CO;2](https://doi.org/10.1175/1520-0442(2001)014<2266:MOITDV>2.0.CO;2).
- Farneti, R., and G. Vallis, 2011: Mechanisms of interdecadal climate variability and the role of ocean–atmosphere coupling. *Climate Dyn.*, **36**, 289–308, <https://doi.org/10.1007/s00382-009-0674-9>.
- Frankcombe, L. M., A. Von der Heydt, and H. Dijkstra, 2010: North Atlantic multidecadal climate variability: An investigation of dominant time scales and processes. *J. Climate*, **23**, 3626–3638, <https://doi.org/10.1175/2010JCLI3471.1>.
- Gent, P., and J. C. McWilliams, 1990: Isopycnal mixing in ocean circulation models. *J. Phys. Oceanogr.*, **20**, 150–155, [https://doi.org/10.1175/1520-0485\(1990\)020<0150:IMIOCM>2.0.CO;2](https://doi.org/10.1175/1520-0485(1990)020<0150:IMIOCM>2.0.CO;2).
- Giering, R., and T. Kaminski, 1998: Recipes for adjoint code construction. *ACM Trans. Math. Softw.*, **24**, 437–474, <https://doi.org/10.1145/293686.293695>.
- He, Y.-C., H. Drange, Y. Gao, and M. Bentsen, 2016: Simulated Atlantic meridional overturning circulation in the 20th century with an ocean model forced by reanalysis-based atmospheric data sets. *Ocean Modell.*, **100**, 31–48, <https://doi.org/10.1016/j.ocemod.2015.12.011>.
- Heimbach, P., C. Hill, and R. Giering, 2005: An efficient exact adjoint of the parallel MIT general circulation model, generated by automatic differentiation. *Future Gen. Comput. Syst.*, **21**, 1356–1371, <https://doi.org/10.1016/j.future.2004.11.010>.
- , C. Wunsch, R. Ponte, G. Forget, C. Hill, and J. Utke, 2011: Timescales and regions of the sensitivity of Atlantic meridional volume and heat transport: Toward observing system design. *Deep-Sea Res.*, **58**, 1858–1879, <https://doi.org/10.1016/j.dsr2.2010.10.065>.
- Huber, M., and L. Zanna, 2017: Drivers of uncertainty in simulated ocean circulation and heat uptake. *Geophys. Res. Lett.*, **44**, 1402–1413, <https://doi.org/10.1002/2016GL071587>.
- Huck, T., A. Colin de Verdiere, and A. Weaver, 1999: Interdecadal variability of the thermohaline circulation in box-ocean models forced by fixed surface fluxes. *J. Phys. Oceanogr.*, **29**, 865–892, [https://doi.org/10.1175/1520-0485\(1999\)029<0865:IVOTTC>2.0.CO;2](https://doi.org/10.1175/1520-0485(1999)029<0865:IVOTTC>2.0.CO;2).
- Jackson, L., K. Peterson, C. Roberts, and R. Wood, 2016: Recent slowing of the Atlantic Overturning Circulation as a recovery from earlier strengthening. *Nat. Geosci.*, **9**, 518–522, <https://doi.org/10.1038/ngeo2715>.
- Jones, D., G. Forget, B. Sinha, S. A. Josey, E. Boland, A. J. S. Meijers, and E. Shuckburgh, 2018: Local and remote influences on the heat content of the Labrador Sea: An adjoint sensitivity study. *J. Geophys. Res. Oceans*, **123**, 2646–2667, <https://doi.org/10.1002/2018JC013774>.
- Kalnay, E., and Coauthors, 1996: The NCEP/NCAR 40-Year Reanalysis Project. *Bull. Amer. Meteor. Soc.*, **77**, 437–471, [https://doi.org/10.1175/1520-0477\(1996\)077<0437:TNYRP>2.0.CO;2](https://doi.org/10.1175/1520-0477(1996)077<0437:TNYRP>2.0.CO;2).
- Kanamitsu, M., W. Ebisuzaki, J. Woollen, S.-K. Yang, J. Hnilo, M. Fiorino, and G. Potter, 2002: NCEP–DOE AMIP-II reanalysis (R-2). *Bull. Amer. Meteor. Soc.*, **83**, 1631–1644, <https://doi.org/10.1175/BAMS-83-11-1631>.
- Klöwer, M., M. Latif, H. Ding, R. J. Greatbatch, and W. Park, 2014: Atlantic meridional overturning circulation and the prediction of North Atlantic sea surface temperature. *Earth Planet. Sci. Lett.*, **406**, 1–6, <https://doi.org/10.1016/j.epsl.2014.09.001>.
- Knight, J., R. Allan, C. Folland, M. Vellinga, and M. Mann, 2005: A signature of persistent natural thermohaline circulation cycles in observed climate. *Geophys. Res. Lett.*, **32**, L20708, <https://doi.org/10.1029/2005GL024233>.
- Kobayashi, S., Y. Ota, Y. Harada, A. Ebita, M. Moriya, H. Onoda, and K. Onogi, 2015: The JRA-55 Reanalysis: General specifications and basic characteristics. *J. Meteor. Soc. Japan*, **93**, 5–48, <https://doi.org/10.2151/jmsj.2015-001>.
- Large, W. G., and S. Pond, 1981: Open ocean momentum flux measurements in moderate to strong winds. *J. Phys. Oceanogr.*, **11**, 324–336, [https://doi.org/10.1175/1520-0485\(1981\)011<0324:OOMFMI>2.0.CO;2](https://doi.org/10.1175/1520-0485(1981)011<0324:OOMFMI>2.0.CO;2).
- , and S. Yeager, 2004: Diurnal to decadal global forcing for ocean and sea-ice models: The data sets and flux climatologies. NCAR Tech. Note NCAR/TN-460+STR, 105 pp., <https://doi.org/10.5065/D6KK98Q6>.
- , and —, 2009: The global climatology of an interannually varying air–sea flux data set. *Climate Dyn.*, **33**, 341–364, <https://doi.org/10.1007/s00382-008-0441-3>.
- , J. C. McWilliams, and S. C. Doney, 1994: Oceanic vertical mixing: A review and a model with a nonlocal boundary layer parameterization. *Rev. Geophys.*, **32**, 363–403, <https://doi.org/10.1029/94RG01872>.
- Latif, M., M. Collins, H. Pohlmann, and N. Keenlyside, 2006: A review of predictability studies of Atlantic sector climate on decadal time scales. *J. Climate*, **19**, 5971–5987, <https://doi.org/10.1175/JCLI3945.1>.
- Levitus, S., J. Antonov, T. Boyer, O. Baranova, H. Garcia, and R. Locarini, 2012: World ocean heat content and thermohaline sea level change (0–2000 m), 1955–2010. *Geophys. Res. Lett.*, **39**, L10603, <https://doi.org/10.1029/2012GL051106>.
- Lilly, J., P. Rhines, M. Visbeck, R. Davis, J. Lazier, F. Schott, and D. Farmer, 1999: Observing deep convection in the Labrador Sea during winter 1994/95. *J. Phys. Oceanogr.*, **29**, 2065–2098, [https://doi.org/10.1175/1520-0485\(1999\)029<2065:ODCITL>2.0.CO;2](https://doi.org/10.1175/1520-0485(1999)029<2065:ODCITL>2.0.CO;2).
- Locarnini, R. A., A. V. Mishonov, J. I. Antonov, T. P. Boyer, H. E. Garcia, O. K. Baranova, M. M. Zweng, and D. R. Johnson, 2010: *Temperature*. Vol. 1, *World Ocean Atlas*, NOAA Atlas NESDIS 68, 184 pp., [ftp://ftp.nodc.noaa.gov/pub/WOA09/DOC/woa09\\_vol1\\_text.pdf](ftp://ftp.nodc.noaa.gov/pub/WOA09/DOC/woa09_vol1_text.pdf).
- Lozier, M. S., and Coauthors, 2017: Overturning in the Subpolar North Atlantic Program: A new international ocean observing system. *Bull. Amer. Meteor. Soc.*, **98**, 737–752, <https://doi.org/10.1175/BAMS-D-16-0057.1>.
- MacMartin, D., E. Tziperman, and L. Zanna, 2013: Frequency domain multimodel analysis of the response of Atlantic meridional overturning circulation to surface forcing. *J. Climate*, **26**, 8323–8340, <https://doi.org/10.1175/JCLI-D-12-00717.1>.
- Marotzke, J., and J. R. Scott, 1999: Convective mixing and the thermohaline circulation. *J. Phys. Oceanogr.*, **29**, 2962–2970, [https://doi.org/10.1175/1520-0485\(1999\)029<2962:CMATTC>2.0.CO;2](https://doi.org/10.1175/1520-0485(1999)029<2962:CMATTC>2.0.CO;2).



- Marshall, D., and H. Johnson, 2013: Propagation of meridional circulation anomalies along western and eastern boundaries. *J. Phys. Oceanogr.*, **43**, 2699–2717, <https://doi.org/10.1175/JPO-D-13-0134.1>.
- Marshall, J., A. Adcroft, C. Hill, L. Perelman, and C. Heisey, 1997a: A finite-volume, incompressible Navier Stokes model for studies of the ocean on parallel computers. *J. Geophys. Res.*, **102**, 5753–5766, <https://doi.org/10.1029/96JC02775>.
- , C. Hill, L. Perelman, and A. Adcroft, 1997b: Hydrostatic, quasi-hydrostatic, and nonhydrostatic ocean modeling. *J. Geophys. Res.*, **102**, 5733–5752, <https://doi.org/10.1029/96JC02776>.
- McCarthy, G., and Coauthors, 2012: Observed interannual variability of the Atlantic meridional overturning circulation at 26.5°N. *Geophys. Res. Lett.*, **39**, L19609, <https://doi.org/10.1029/2012GL052933>.
- , and Coauthors, 2015: Measuring the Atlantic meridional overturning circulation at 26°N. *Prog. Oceanogr.*, **130**, 91–111, <https://doi.org/10.1016/j.pocean.2014.10.006>.
- Msadek, R., and Coauthors, 2014: Predicting a decadal shift in North Atlantic climate variability using the GFDL forecast system. *J. Climate*, **27**, 6472–6496, <https://doi.org/10.1175/JCLI-D-13-00476.1>.
- Nikurashin, M., and G. Vallis, 2012: A theory of the interhemispheric meridional overturning circulation and associated stratification. *J. Phys. Oceanogr.*, **42**, 1652–1667, <https://doi.org/10.1175/JPO-D-11-0189.1>.
- Pawson, S., and M. Fiorino, 1999: A comparison of reanalyses in the tropical stratosphere. Part 3: Inclusion of the pre-satellite data era. *Climate Dyn.*, **15**, 241–250, <https://doi.org/10.1007/s003820050279>.
- Pickart, R., K. Våge, G. Moore, I. Renfrew, M. Ribergaard, and H. Davies, 2008: Convection in the western North Atlantic sub-polar gyre: Do small-scale wind events matter? *Arctic-Subarctic Ocean Fluxes*, R. Dickson, J. Meincke, and P. Rhines, Eds., Springer, 629–652.
- Pillar, H., 2013: Sensitivity of the Atlantic meridional overturning circulation to surface forcing. Ph.D. thesis, University of Oxford, 262 pp., <https://ora.ox.ac.uk/objects/uuid:42366dc7-e699-4349-95d2-89a97033d957>.
- , P. Heimbach, H. Johnson, and D. Marshall, 2016: Dynamical attribution of recent variability in Atlantic overturning. *J. Climate*, **29**, 3339–3352, <https://doi.org/10.1175/JCLI-D-15-0727.1>.
- Polo, I., J. Robson, R. Sutton, and M. A. Balmaseda, 2014: The importance of wind and buoyancy forcing for the boundary density variations and the geostrophic component of the AMOC at 26°N. *J. Phys. Oceanogr.*, **44**, 2387–2408, <https://doi.org/10.1175/JPO-D-13-0264.1>.
- Redi, M., 1982: Oceanic isopycnal mixing by coordinate rotation. *J. Phys. Oceanogr.*, **12**, 1154–1158, [https://doi.org/10.1175/1520-0485\(1982\)012<1154:OIMBCR>2.0.CO;2](https://doi.org/10.1175/1520-0485(1982)012<1154:OIMBCR>2.0.CO;2).
- Roberts, C., and Coauthors, 2013: Atmosphere drives recent interannual variability of the Atlantic meridional overturning circulation at 26.5°N. *Geophys. Res. Lett.*, **40**, 5164–5170, <https://doi.org/10.1002/grl.50930>.
- Robson, J., R. Sutton, K. Lohmann, D. Smith, and M. Palmer, 2012a: Causes of the rapid warming of the North Atlantic Ocean in the mid-1990s. *J. Climate*, **25**, 4116–4134, <https://doi.org/10.1175/JCLI-D-11-00443.1>.
- , —, and D. M. Smith, 2012b: Initialized decadal prediction of the rapid warming of the North Atlantic Ocean in the mid 1990s. *Geophys. Res. Lett.*, **39**, L19713, <https://doi.org/10.1029/2012GL053370>.
- Santer, B. D., J. J. Hnilo, T. M. L. Wigley, J. S. Boyle, C. Doutriaux, M. Fiorino, D. E. Parker, and K. E. Taylor, 1999: Uncertainties in observationally based estimates of temperature change in the free atmosphere. *J. Geophys. Res.*, **104**, 6305–6333, <https://doi.org/10.1029/1998JD200096>.
- , and Coauthors, 2004: Identification of anthropogenic climate change using a second-generation reanalysis. *J. Geophys. Res.*, **109**, D21104, <https://doi.org/10.1029/2004JD005075>.
- Shaffrey, D., and Coauthors, 2017: Decadal predictions with the HiGEM high resolution global coupled climate model: Description and basic evaluation. *Climate Dyn.*, **48**, 297–311, <https://doi.org/10.1007/s00382-016-3075-x>.
- Simmons, A., K. Willett, P. Jones, P. Thorne, and D. Dee, 2010: Low-frequency variations in surface atmospheric humidity, temperature, and precipitation: Inferences from reanalyses and monthly gridded observational data sets. *J. Geophys. Res.*, **115**, D01110, <https://doi.org/10.1029/2009JD012442>.
- Smeed, D., and Coauthors, 2014: Observed decline of the Atlantic meridional overturning circulation 2004–2012. *Ocean Sci.*, **10**, 29–38, <https://doi.org/10.5194/os-10-29-2014>.
- Stammer, D., M. Balmaseda, P. Heimbach, A. Khl, and A. Weaver, 2016: Ocean data assimilation in support of climate applications: Status and perspectives. *Annu. Rev. Mar. Sci.*, **8**, 491–518, <https://doi.org/10.1146/annurev-marine-122414-034113>.
- Te Raa, L., and H. Dijkstra, 2002: Instability of the thermohaline ocean circulation on interdecadal timescales. *J. Phys. Oceanogr.*, **32**, 138–160, [https://doi.org/10.1175/1520-0485\(2002\)032<0138:IOTTOC>2.0.CO;2](https://doi.org/10.1175/1520-0485(2002)032<0138:IOTTOC>2.0.CO;2).
- Thomas, M. D., and X. Zhai, 2013: Eddy induced variability of the meridional overturning circulation in a model of the North Atlantic. *Geophys. Res. Lett.*, **40**, 2742–2747, <https://doi.org/10.1002/grl.50532>.
- , A.-M. Tréguier, B. Blanke, J. Deshayes, and A. Voldoire, 2015: A Lagrangian method to isolate the impacts of mixed layer subduction on the meridional overturning circulation in a numerical model. *J. Climate*, **28**, 7503–7517, <https://doi.org/10.1175/JCLI-D-14-00631.1>.
- Thompson, D., J. Kennedy, J. Wallace, and P. Jones, 2008: A large discontinuity in the mid-twentieth century in observed global-mean surface temperature. *Nature*, **453**, 646–649, <https://doi.org/10.1038/nature06982>.
- Thorne, P., and R. Vose, 2010: Reanalyses suitable for characterizing long-term trends. *Bull. Amer. Meteor. Soc.*, **91**, 353–361, <https://doi.org/10.1175/2009BAMS2858.1>.
- Uppala, S. M., and Coauthors, 2005: The ERA-40 re-analysis. *Quart. J. Roy. Meteor. Soc.*, **131**, 2961–3012, <https://doi.org/10.1256/qj.04.176>.
- Våge, K., and Coauthors, 2009: Surprising return of deep convection to the subpolar North Atlantic Ocean in winter 2007–2008. *Nat. Geosci.*, **2**, 67–72, <https://doi.org/10.1038/ngeo382>.
- Wunsch, C., and P. Heimbach, 2013a: Dynamically and kinematically consistent global ocean circulation and ice state estimates. *Ocean Circulation and Climate: A 21st Century Perspective*, G. Siedler et al., Eds., Elsevier, 553–579.
- , and —, 2013b: Two decades of the Atlantic overturning circulation: Anatomy, variations, extremes, prediction, and overcoming its limitations. *J. Climate*, **26**, 7167–7186, <https://doi.org/10.1175/JCLI-D-12-00478.1>.
- Yeager, S., and G. Danabasoglu, 2012: Sensitivity of the Atlantic meridional overturning circulation variability to parameterized

- Nordic Sea overflows in CCSM4. *J. Climate*, **25**, 2077–2103, <https://doi.org/10.1175/JCLI-D-11-00149.1>.
- , and —, 2014: The origins of late-twentieth-century variations in the large-scale North Atlantic circulation. *J. Climate*, **27**, 3222–3247, <https://doi.org/10.1175/JCLI-D-13-00125.1>.
- , A. Karspeck, G. Danabasoglu, J. Tribbia, and H. Teng, 2012: A decadal prediction case study: Late twentieth-century North Atlantic Ocean heat content. *J. Climate*, **25**, 5173–5189, <https://doi.org/10.1175/JCLI-D-11-00595.1>.
- , —, and —, 2015: Predicted slowdown in the rate of Atlantic sea ice loss. *Geophys. Res. Lett.*, **42**, 10 704–10 713, <https://doi.org/10.1002/2015GL065364>.
- Zanna, L., P. Heimbach, A. Moore, and E. Tziperman, 2012: Upper ocean singular vectors of the North Atlantic climate with implications for linear predictability and variability. *Quart. J. Roy. Meteor. Soc.*, **138**, 500–513, <https://doi.org/10.1002/qj.937>.
- Zhai, X., H. L. Johnson, and D. P. Marshall, 2014: A simple model of the response of the Atlantic to the North Atlantic Oscillation. *J. Climate*, **27**, 4052–4069, <https://doi.org/10.1175/JCLI-D-13-00330.1>.
- Zhang, L., and C. Wang, 2013: Multidecadal North Atlantic sea surface temperature and Atlantic meridional overturning circulation variability in CMIP5 historical simulations. *J. Geophys. Res. Oceans*, **118**, 5772–5791, <https://doi.org/10.1002/jgrc.20390>.
- Zhang, R., and T. Delworth, 2005: Simulated tropical response to a substantial weakening of the Atlantic thermohaline circulation. *J. Climate*, **18**, 1853–1860, <https://doi.org/10.1175/JCLI3460.1>.
- Zhao, J., and W. Johns, 2014: Wind-forced interannual variability of the Atlantic meridional overturning circulation at 26.5°N. *J. Geophys. Res. Oceans*, **119**, 2403–2419, <https://doi.org/10.1002/2013JC009407>.